

1 **Ozone variability in the troposphere and the stratosphere from the first six years of IASI**
2 **observations (2008-2013)**

3 C. Wespes¹, D. Hurtmans¹, L.K. Emmons², S. Safieddine^{3*}, C. Clerbaux^{1,3}, D. P. Edwards² and
4 P.-F. Coheur¹

5 ¹Spectroscopie de l'Atmosphère, Service de Chimie Quantique et Photophysique, Université
6 Libre de Bruxelles (U.L.B.), Brussels, Belgium

7 ²National Center for Atmospheric Research, Boulder, CO, USA

8 ³Sorbonne Universités, UPMC Univ. Paris 06; Université Versailles St-Quentin; CNRS/INSU,
9 LATMOS-IPSL, Paris, France

10 *Now at Department of Civil and Environmental Engineering, Institute of Technology,
11 Cambridge, Massachusetts, United States

12

13 **Abstract**

14 In this paper, we assess how daily ozone (O₃) measurements from the Infrared Atmospheric
15 Sounding Interferometer (IASI) on the MetOp-A platform can contribute to the analyses of the
16 processes driving O₃ variability in the troposphere and the stratosphere and, in the future, to the
17 monitoring of long-term trends. The temporal evolution of O₃ during the first 6 years of IASI
18 (2008-2013) operation is investigated with multivariate regressions separately in four different
19 layers (ground-300 hPa, 300-150 hPa, 150-25 hPa, 25-3 hPa), by adjusting to the daily time
20 series averaged in 20° zonal bands, seasonal and linear trend terms along with important
21 geophysical drivers of O₃ variation (e.g. solar flux, quasi biennial oscillations). The regression
22 model is shown to perform generally very well with a strong dominance of the annual harmonic
23 terms and significant contributions from O₃ drivers, in particular in the equatorial region where
24 the QBO and the solar flux contribution dominate. More particularly, despite the short period of
25 IASI dataset available to now, two noticeable statistically significant apparent trends are inferred
26 from the daily IASI measurements: a positive trend in the upper stratosphere (e.g. 1.74±0.77
27 DU/yr between 30°S-50°S) which is consistent with other studies suggesting a turnaround for
28 stratospheric O₃ recovery, and a negative trend in the troposphere at the mid-and high northern

29 latitudes (e.g. -0.26 ± 0.11 DU/yr between 30°N-50°N), especially during summer and probably
30 linked to the impact of decreasing ozone precursor emissions. The impact of the high temporal
31 sampling of IASI on the uncertainty in the determination of O₃ trend has been further explored
32 by performing multivariate regressions on IASI monthly averages and on ground-based FTIR
33 measurements.

34

35 **1 Introduction**

36 Global climate change is one of the most important environmental problems of today and
37 monitoring the behavior of the atmospheric constituents (radiatively active gases and those
38 involved in their chemical production) is key to understand the present climate and apprehend
39 future climate changes. Long-term measurements of these gases are necessary to study the
40 evolution of their abundance, changing sources and sinks in the atmosphere.

41

42 As a reactive trace gas present simultaneously in the troposphere and in the stratosphere, O₃
43 plays a significant role in atmospheric radiative forcing, atmospheric chemistry and air quality.
44 In the stratosphere, O₃ is sensitive to changes in (photo-)chemical and dynamical processes and,
45 as a result, undergoes large variations on seasonal and annual time scales. Measurements of O₃
46 total column have indicated a downward trend in stratospheric ozone over the period from 1980s
47 to the late 1990s relative to the pre-1980 values, which is due to the growth of the reactive
48 bromine and chlorine species following anthropogenic emissions during that period (WMO,
49 2003). In response to the 1987 Montreal Protocol and its amendments, with a reduction of the
50 Ozone-Depleting Substances (ODS; Newchurch et al., 2003), a recovery of stratospheric ozone
51 concentrations to the pre-1980 values is expected (Hofmann, 1996). While earlier works have
52 debated a probable turnaround for the ozone hole recovery (e.g. Hadjinicolaou et al., 2005;
53 Reinsel et al., 2002; Stolarski and Frith, 2006), WMO already indicated in 2007 that the total
54 ozone in the 2002-2005 period was no longer decreasing, reflecting such a turnaround. Since
55 then several studies have shown successful identification of ozone recovery over Antarctica and
56 over northern latitudes (e.g. Mäder et al., 2010; Salby et al., 2011; WMO, 2011; Kuttippurath et
57 al., 2013; Knibbe et al., 2014; Shepherd et al., 2014). Nevertheless, the most recent papers as
58 well as the WMO 2014 ozone assessment have warned, because of possible underestimation of

59 the true uncertainties in the ozone trends attributed to decreasing Effective Equivalent
60 Stratospheric Chlorine (EESC), against overly optimistic conclusions with regard to a possible
61 increase in Antarctic stratospheric ozone (Kramarova et al., 2014 ; WMO, 2014; Knibbe et al.,
62 2014; de Laat et al., 2015; Kuttippurath et al., 2015; Varai et al., 2015). The causes of the
63 observed stratospheric O₃ changes are hard to isolate and remain uncertain precisely considering
64 the contribution of dynamical variability to the apparent trend and the limitations of current
65 chemistry-climate models to reproduce the observations. The assessment of ozone trends in the
66 troposphere is even more challenging due to the influence of many simultaneous processes (e.g.
67 emission of precursors, long-range transport, stratosphere-troposphere exchanges –STE–), which
68 are all strongly variable temporally and spatially (e.g. Logan et al., 2012; Hess and Zbinden,
69 2013; Neu et al., 2014). Overall, there are still today large differences in the value of the O₃
70 trends determined from independent studies and datasets (mostly from ground-based and satellite
71 observations) in both the stratosphere and the troposphere (e.g. Oltmans et al., 1998; 2006;
72 Randel and Wu, 2007; Gardiner et al., 2008; Vigouroux et al., 2008; Jiang et al., 2008; Kyrölä et
73 al., 2010; Vigouroux et al., 2014). In order to improve on this and because O₃ has been
74 recognized as a Global Climate Observing System (GCOS) Essential Climate Variables (ECVs),
75 the scientific community has underlined the need of acquiring high quality global, long-term and
76 homogenized ozone profile records from satellites (Randel and Wu, 2007; Jones et al., 2009;
77 WMO, 2007; 2011; 2014). This specifically has resulted in the ESA Ozone Climate Change
78 Initiative (O₃-CCI; <http://www.esa-ozone-cci.org/>).

79
80 The Infrared Atmospheric Sounding Interferometer (IASI) onboard the polar orbiting MetOp,
81 with its unprecedented spatiotemporal sampling of the globe, its high radiometric stability and
82 the long duration of its program (3 successive instruments to cover 15 years) provides in
83 principle an excellent means to contribute to the analyses of the O₃ variability and trends. This is
84 further strengthened by the possibility of using IASI measurements to discriminate O₃
85 distributions and variability in the troposphere and the stratosphere, as shown in earlier studies
86 (Boynard et al., 2009; Wespes et al., 2009; Dufour et al, 2010 ; Barret et al., 2011; Scannell et
87 al., 2012; Wespes et al., 2012; Safieddine et al., 2013). Here, we use the first 6 years (2008-
88 2013) of the new O₃ dataset provided by IASI on MetOp-A to perform a first analysis of the O₃

89 time development in the stratosphere and in the troposphere. This is achieved globally by using
90 zonal averages in 20° latitude bands and a multivariate linear regression model which accounts
91 for various natural cycles affecting O₃. We also explore in this paper to which extent the
92 exceptional temporal sampling of IASI can counterbalance the short period of data available for
93 assessing trends in partial columns.

94

95 In section 2, we give a short description of IASI and of the O₃ retrieved columns used here.
96 Section 3 details the multivariate regression model used for fitting the time series. In Section 4,
97 we evaluate how the ozone natural variability is captured by IASI and we present the time
98 evolution of the retrieved O₃ profiles and of four partial columns (Upper Stratosphere –UST–;
99 Middle-Low Stratosphere –MLST–; Upper Troposphere Lower Stratosphere –UTLS–; Middle-
100 Low Troposphere –MLT–) using 20-degree latitudinal averages on a daily basis. The apparent
101 dynamical and chemical processes in each latitude band and vertical layer are then analyzed on
102 the basis of the multiple regression results using a series of common geophysical variables. The
103 “standard” contributors in the fitted time series, as well as a linear trend term, are analyzed in the
104 specified altitude layers. Finally, the trends inferred from IASI are compared against those from
105 FTIR for six stations in the northern hemisphere.

106

107 **2 IASI measurements and retrieval method**

108 IASI measures the thermal infrared emission of the Earth-atmosphere between 645 and 2760
109 cm⁻¹ with a field of view of 2×2 circular pixels on the ground, each of 12 km diameter at nadir.
110 The IASI measurements are taken every 50 km along the track of the satellite at nadir, but also
111 across-track over a swath width of 2200 km. IASI provides a global coverage twice a day with
112 overpass times at 9:30 and 21:30 mean local solar time. The instrument is also characterized by a
113 high spectral resolution which allows the retrieval of numerous gas-phase species (e.g. Clerbaux
114 et al., 2009; Clarisse et al., 2012).

115

116 Ozone profiles are retrieved with the Fast Optimal Retrievals on Layers for IASI (FORLI)
117 software developed at ULB/LATMOS. FORLI relies on a fast radiative transfer and on a
118 retrieval methodology based on the Optimal Estimation Method (Rodgers, 2000). In the version

119 used in this study (FORLI-O₃ v20100815), the O₃ profile is retrieved for individual IASI
120 measurement on a uniform 1 km vertical grid on 40 layers from surface up to 40 km. The a priori
121 information (a priori profile and a priori covariance matrix) is built from the
122 Logan/Labow/McPeters climatology (McPeters et al., 2007) and only one single O₃ a priori
123 profile and variance-covariance matrix are used. The retrieval parameters and performances are
124 detailed in Hurtmans et al. (2012). The FORLI-O₃ profiles and/or total and partial columns have
125 undergone validation using available ground-based, aircraft, O₃ sonde and other satellite
126 observations (Anton et al., 2011; Dufour et al., 2012; Gazeaux et al., 2012; Parrington et al.,
127 2012; Pommier et al., 2012; Scannell et al., 2012; Oetjen et al., 2014). Generally, the results
128 show good agreements between FORLI-O₃ and independent measurements with a low bias
129 (<10%) in the total column and in the vertical profile, except in UTLS where a positive bias of
130 10-15% is reported (Dufour et al., 2012; Gazeaux et al., 2012; Oetjen et al., 2014).

131
132 In this study, only daytime O₃ IASI observations from good spectral fits (RMS of the spectral
133 residual lower than 3.5×10^{-8} W/cm².sr.cm⁻¹) have been analyzed. Daytime IASI observations
134 (determined with a solar zenith angle to the sun < 80°) are characterized by a better vertical
135 sensitivity to the troposphere associated with a higher surface temperature and a higher thermal
136 contrast (Clerbaux et al., 2009; Boynard et al., 2009). Furthermore, cloud contaminated scenes
137 with cloud cover < 13% (Hurtmans et al., 2012) were removed using cloud information from the
138 Eumetcast operational processing (August et al., 2012).

139
140 An example of typical FORLI-O₃ averaging kernel functions for one mid-latitude observation in
141 July (45°N/66°E) is represented on Fig.1. The layers have been defined as: ground-300hPa
142 (MLT), 300-150hPa (UTLS), 150-25 hPa (MLST) and above 25 hPa (UST), so that they are
143 characterized by a DOFS (Degrees Of Freedom for Signal) close to 1 with a maximum
144 sensitivity approximatively in the middle of the layers, except for the 300-150 hPa layer which
145 has a reduced sensitivity. Taken globally, the DOFS for the entire profile ranges from ~2.5 in
146 cold polar regions to ~4.5 in hot tropical regions, depending mostly on surface temperature, with
147 a maximum sensitivity in the upper troposphere and in the lower stratosphere (Hurtmans et al.,
148 2012). In the MLT, the maximum of sensitivity is around 4–8 km altitude for almost all

149 situations (Wespes et al., 2012). The sharp decrease of sensitivity down to the surface is inherent
150 to nadir thermal IR sounding in cases of low surface temperature or low thermal contrast and
151 indicates that the retrieved information principally comes from the a priori in the lowest layer.
152 Figure 2 presents July 2010 global maps of averaged FORLI-O₃ partial columns for two partial
153 layers (MLT and MLST), and of the associated DOFS and *a priori* contribution (calculated as
154 $X_a - \mathbf{A}(X_a)$, where X_a is the *a priori* profile and \mathbf{A} , the averaging kernel matrix, following the
155 formalism of Rodgers (2000)). The two layers exhibit different sensitivity patterns: in the MLT,
156 the DOFS typically range from 0.4 in the cold polar regions to 1 in regions characterized by high
157 thermal contrast with medium humidity, such as the mid-latitude continental Northern
158 Hemisphere (N.H.) (Clerbaux et al., 2009). Lower DOFS values in the intertropical belt are
159 explained by overlapping water vapor lines. In contrast, the DOFS for the MLST are globally
160 almost constant and close to one, with only slightly lower values (0.9) over polar regions. The *a*
161 *priori* contribution is anti-correlated with the sensitivity, as expected. It ranges between a few %
162 to ~30% and does not exceed 20% on 20° zonal averages in the troposphere (see Supporting
163 Information; Fig. S3, dashed lines), while the a priori contribution is smaller than ~12% in the
164 middle stratosphere. These findings indicate that the IASI MLST time series should accurately
165 represent stratospheric variations, while the time series in the troposphere may reflect to some
166 extent variations from the upper layers in addition to the real variability in the troposphere. In
167 order to quantify this effect, the contribution of the stratosphere into the tropospheric ozone as
168 seen by IASI has been estimated with a global 3-D chemical transport model (MOZART-4).
169 Details of the model-observation comparisons can be found in the Supplement (see Fig. S2 and
170 S3). We interestingly show that the stratospheric contribution to the MLT columns measured by
171 IASI varies between 30% and 60%, depending on latitude and season (Fig. S5). The limited
172 vertical sensitivity of IASI contributes to this by a smaller part (~10%-20%) than the natural
173 stratospheric influence (~20% to 45%) (See Fig. S4 and S5). In addition, we find that the
174 contribution of the natural variability (from both the troposphere and the stratosphere) on the
175 MLT O₃ columns is larger than 50% everywhere. In the 30N-50N band where the DOFS is the
176 largest (See Fig.2 (b)), this contribution reaches ~85% from which ~25-35% originates from the
177 stratosphere and ~55% from the troposphere (Fig.S6 (a) and (b)). Nevertheless, the

178 contamination of IASI MLT O₃ with variations in stratospheric O₃ has to be kept in mind when
 179 analyzing IASI MLT O₃.

180 **3 Fitting method**

181 **3.1. Statistical model**

182 In order to characterize the changes in ozone measured by IASI and to allow a proper separation
 183 of trend, we use a multiple linear regression model accounting for a linear trend and for inter-
 184 annual, seasonal and non-seasonal variations related to physical processes that are known to
 185 affect the ozone records. More specifically, the time series analysis is based on the fitting of
 186 daily (or monthly) median partial columns in different latitude band following:

$$187 \quad O_3(t) = Cst + x_1 \cdot trend + \sum_{n=1,2} [a_n \cdot \cos(n\omega t) + b_n \cdot \sin(n\omega t)] + \sum_{j=2}^m x_j X_{norm,j}(t) + \varepsilon(t) \quad (1)$$

188 where t is the number of days (or months), x_1 is the 6-year trend coefficient in the data, $\omega =$
 189 $2\pi/365.25$ for the daily model (or $2\pi/12$ for the monthly model) and $X_{norm,j}$ are independent
 190 geophysical variables, the so-called “explanatory variables” or “proxies”, which are in this study
 191 normalized over the period of IASI observation (2008-2013), as:

$$192 \quad X_{norm}(t) = 2[X(t) - X_{median}] / [X_{max} - X_{min}] \quad (2)$$

193 $\varepsilon(t)$ in Eq. (1) represents the residual variation which is not described by the model and which is
 194 assumed to be autoregressive with time lag of 1 day (or 1 month). The constant term (Cst) and
 195 the coefficients a_n, b_n, x_j are estimated by least-squares method and their standard errors (σ_e)
 196 are calculated from the covariance matrix of the coefficients and corrected to take into account
 197 the uncertainty due to the autocorrelation of the noise residual as discussed in Santer et al. (2000)
 198 and references therein:

$$199 \quad \sigma_e^2 = (Y^T Y)^{-1} \cdot \frac{\sum [O_3(t) - yY(t)]^2}{n - m} \cdot \frac{1 + \Phi}{1 - \Phi} \quad (3)$$

200 Where Y is the matrix with the covariates ($trend, \cos(n\omega t), \sin(n\omega t), X_{norm,j}$) sorted by
 201 column, y is the vector of the regression coefficients corresponding to the columns of Y , n is the

202 number of daily (or monthly) data points in the time series, m is the number of the fitted
203 parameters, and Φ is the lag-1 autocorrelation of the residuals.

204

205 The median is used as a statistical average since it is more robust against the outliers than the
206 normal mean (Kyrölä et al., 2006; 2010). Note that, similarly to Kyrölä et al. (2010), the model
207 has been applied on O_3 mixing ratios rather than on partial columns but without significant
208 improvement on the fitting residuals and R values.

209

210 **3.2. Geophysical variables**

211 In Eq. (1), harmonic time series with a period of a year and a half year are used to account for the
212 Brewer-Dobson circulation and the solar insolation (a_1 and b_1 coefficients), and for the
213 meridional circulation (a_2 and b_2 coefficients), respectively (Kyrölä et al., 2010). While these
214 effects are of a periodic nature, the geophysical variables (X_j) are used here to parameterize the
215 ozone variations on non-seasonal timescales. The chosen proxies are $F_{10.7}$, QBO^{10} , QBO^{30} , $ENSO$,
216 NAO/AAO , the first three being the most commonly used (“standard”) proxies to describe the
217 natural ozone variability, i.e. the solar radio flux at 10.7 cm and the quasi-biennial oscillation
218 (QBO) which is represented by two orthogonal zonal components of the equatorial stratospheric
219 wind measured at 10 hPa and 30 hPa, respectively (e.g. Randel and Wu, 2007). The three other
220 proxies, $ENSO$, NAO and AAO , are used to account for other important fluctuating dynamical
221 features: the El Niño/Southern Oscillation, the North Atlantic Oscillation and the Antarctic
222 Oscillation, respectively. Table 1 lists the selected proxies, their sources and their resolutions.
223 The time series of these proxies normalized over the 2000-2013 period following Eq. 2 are
224 shown in Fig.3 (a) and (b) and they are shortly described hereafter:

225 - *Solar flux*: the F10.7 cm solar radio flux is an excellent indicator of solar activity and is
226 commonly used to represent the 11 year solar cycle. It is available from continuous routine
227 consistent measurements at the Penticton Radio Observatory in British Columbia which are
228 corrected for the variable Sun-Earth distance resulting from the eccentric orbit of the Earth
229 around the Sun. Over the period 2008-2013, the radio solar flux increases from about 65 units in
230 2008 to 180 units in 2013 and is characterized by a specific daily “fingerprint” (see Fig.3 (a)).
231 Note that because the period of IASI observations does not cover a full 11 year solar cycle, it

232 could affect the determination of the trend in the regression procedure. The difficulty in
233 discriminating the solar flux and linear trend terms is a known problem for such multivariate
234 regression: it feeds into their uncertainties and it can lead to biases in the coefficients
235 determination (e.g. Soukharev et al., 2006).

236 - *QBO terms*: The QBO of the equatorial winds is a main component of the dynamics of the
237 tropical stratosphere (Chipperfield et al., 1994; 2003; Randel and Wu, 1996; 2007; Logan et al.,
238 2003; Tian et al., 2006; Fadnavis and Beig, 2009; Hauchecorne et al., 2010). It strongly
239 influences the distributions of stratospheric O₃ propagating alternatively westerly and easterly
240 with a mean period of 28 to 29 months. Positive and negative vertical gradients alternate
241 periodically. At the top of the vertical QBO domain, there is a predominance of easterlies, while,
242 at the bottom, westerly winds are more frequent. In order to account for the out-of-phase
243 relationship between the QBO periodic oscillations in the upper and in the lower stratosphere,
244 orthogonal zonal winds measured at 10hPa (Fig.3a; orange) and 30hPa (Fig.3a; green) by the
245 ground-station in Singapore have been considered here (Randel and Wu, 1996; Hood and
246 Soukharev, 2006).

247 - *NAO, AAO and ENSO*: The El Niño/Southern Oscillation is represented by the 3-month
248 running mean of Sea Surface Temperature (SST) anomalies (in degrees Celsius) in the Niño
249 region 3.4 (region bounded by 120°W-170°W and 5°S- 5°N). Raw data are taken from marine
250 ships and buoys observations. The North Atlantic and Antarctic Oscillations are described by the
251 daily (or monthly) NAO and AAO indices which are constructed from the daily (or monthly)
252 mean 500-hPa height anomalies in the 20°N-90°N region and 700-hPa height anomalies in the
253 20°S-90°S region, respectively. Detailed information for these proxies can be found in
254 <http://www.cpc.ncep.noaa.gov/>. These proxies describe important dynamical features which
255 affect ozone distributions in both the troposphere and the lower stratosphere (e.g. Weiss et al.,
256 2001, Frossard et al., 2013; Rieder et al., 2013; and references therein). The daily or 3-monthly
257 average indexes used to parameterize these fluctuations are shown in Fig. 3 (b). The NAO and
258 AAO indexes are used for the N.H. and the S.H. (Southern Hemisphere), respectively (both are
259 used for the equatorial band). These proxies have been included in the statistical model for
260 completeness even if they are expected to only have a weak apparent contribution to the IASI
261 ozone time series due to their large spatial variability in a zonal band (e.g. Frossard et al., 2013;

262 Rieder et al., 2013). We have verified that including a typical time-lag relation between ozone
263 and the ENSO variable from 0 to 4 months did not improve the regression model in terms of
264 residuals and uncertainty of the fitted parameters. As a consequence, a time-lag has not been
265 taken into account in our study.

266 - *Effective equivalent stratospheric chlorine (EESC)*: The EESC is a common proxy used for
267 describing the influence of the ODS in O₃ variations. However, because the IASI time series
268 starts several years after the turnaround for the ozone hole recovery in 1996/1997 (WMO, 2010),
269 their influence is not represented by a dedicated proxy but is rather accounted for by the linear
270 trend term.

271
272 Even if some of the above proxies are only specific to processes occurring in the stratosphere, we
273 adopt the same approach (geophysical variables, model and regression procedure) for adjusting
274 the IASI O₃ time series in the troposphere. This proves useful in particular to account for the
275 stratospheric contribution to the tropospheric layer (~30-60%; see Section 2 and Supporting
276 Information, Fig. S5) due to stratosphere-troposphere exchanges (STE) and to the fact that this
277 tropospheric layer is not perfectly decorrelated from the stratosphere. This has to be kept in mind
278 when analyzing the time series in the troposphere in Section 4. Specific processes in the
279 troposphere such as emissions of ozone precursors, long-range transport and in situ chemical
280 processing are taken into account in the model in the harmonic and the linear trend terms of the
281 Eq. 1 (e.g. Logan et al., 2012). Including harmonic terms having 4- and 3-month periods in the
282 model has been tested to describe O₃ dependency on shorter scales (e.g. Gebhardt et al., 2014),
283 but this did not improved the results in terms of residuals and uncertainty of correlation
284 coefficients.

285 286 **3.3. Iterative backward variable selection**

287 Similarly to previous studies (e.g. Steinbrecht et al., 2004; Mäder et al. 2007, 2010; Knibbe et al.,
288 2014), we perform an iterative stepwise backward elimination approach, based on p-values of the
289 regression coefficients for the rejection, to select the most relevant combination of the above
290 described regression variables (harmonic, linear and explanatory) to fit the observations. The
291 minimum p-value for a regression term to be removed (exit tolerance) is set at 0.05, which

292 corresponds to a significance of 95%. The initial model which includes all regression variables is
293 fitted first. Then, at each iteration, the variables characterized by p-values larger than 5% are
294 rejected. At the end of the iterative process, the remaining terms are considered to have
295 significant influence on the measured O₃ variability while the rejected variables are considered to
296 be non-significant. The correction accounting for the autocorrelation in the noise residual is then
297 applied to give more confidence in the coefficients determination.

298

299 **4 Ozone variations observed by IASI**

300 In this section, we first examine the ozone variations in IASI time series during 2008-2013 in the
301 four layers defined in the troposphere and the stratosphere to match the IASI sensitivity (Section
302 2). The performance of the multiple linear model is evaluated in subsection 4.2 in terms of
303 residuals errors, regression coefficients and associated uncertainties determined from the
304 regression procedure (Section 3). Based on this, we characterize the principal physical processes
305 that affect the IASI ozone records. Finally, the ability of IASI to derive apparent trends is
306 examined in sub-section 4.3.

307

308 **4.1 O₃ time series from IASI**

309 Figure 4 (a) shows the time development of daily O₃ number density over the entire altitude
310 range of the retrieved profiles based on daily medians. The time series cover the six years of
311 available IASI observations and are separated in three 20-degree latitude belts: 30°N-50°N (top
312 panel), 10°N-10°S (middle panel) and 30°S-50°S (bottom panel). The figure shows the well-
313 known seasonal cycle at mid-latitudes in the troposphere and the stratosphere with maxima
314 observed in spring-summer and in winter-spring, respectively, and a strong stability of ozone
315 layers with time in the equatorial belt. At high latitudes of both hemispheres, the high ozone
316 concentrations and the large amplitude of the seasonal cycle observed in MLST and UTLS are
317 mainly the consequence of the large-scale downward poleward Brewer-Dobson circulation
318 which is prominent in late winter below 25 km.

319

320 Figure 4 (b) presents the estimated statistical uncertainty on the O₃ profiles retrieved from
321 FORLI. This total error depends on the latitude and the season, reflecting, amongst other, the

322 influence of signal intensity, of interfering water lines and of thermal contrast under certain
323 conditions (e.g. temperature inversion, high thermal contrast at the surface). It usually ranges
324 between 10 and 30% in the troposphere and in the UTLS (Upper Troposphere-Lower
325 Stratosphere), except in the equatorial belt due to the low O₃ amounts (see Fig.4 (a)) which leads
326 to larger relative errors. The retrieval errors are usually less than 5% in the stratosphere.

327
328 The relative variability (given as the standard deviation) of the daily median O₃ time series
329 presented in Fig.4 (a) is shown in Fig.5, as a function of time and altitude. It is worth noting that,
330 except in the UTLS over the equatorial band, the variability is larger than the estimated retrieval
331 errors of the FORLI-O₃ data (~25% vs ~15% and ~10% vs ~5%, on average over the troposphere
332 and the stratosphere, respectively), reflecting that the high natural temporal variability of O₃ in
333 zonal bands is well captured with FORLI (Dufour et al., 2012; Hurtmans et al., 2012). The
334 standard deviation is larger in the troposphere and in the stratosphere below 20 km where
335 dynamic processes play an important role. The largest values (>70% principally in the northern
336 latitudes during winter) are measured around 9-15km altitude. They highlight the influence of
337 tropopause height variations and the STE processes. In the stratosphere, the variability is always
338 lower than 20% and becomes negligible in the equatorial region. Interestingly, the lowest
339 troposphere of the N.H. (below 700 hPa; <4km) is marked by an increase in both O₃
340 concentrations (Fig. 4a) and standard deviations (between ~30% and ~45%) in spring-summer,
341 the latter being larger than the total retrieval error (less than 25%, see Fig. 4 (b)). The lower
342 tropospheric column (e.g. ground-700 hPa) can generally not well be discriminated because of
343 the weak sensitivity of IASI in the lowermost layers (Section 2). However, the measurements in
344 northern mid-latitudes in spring-summer are characterized by a larger sensitivity. In the ground-
345 700hPa columns, we find that the apriori contributions do not exceed 40% and they range
346 between 10% and 20% over the continental regions. In addition, the stratosphere-troposphere
347 exchanges are usually the weakest in summer. The stratospheric contributions into the IASI
348 MLT columns are estimated to be the lowest in the summer mid-latitudes N.H. (e.g. ~35% in
349 the 30°N-50°N band; See Fig. S5 (b) of the Supplement) and, as mentioned in Section 2, the
350 real natural contribution originating from the troposphere reaches ~55% (cfr Fig.S6 (b) in
351 Supplement). This certainly helps in detecting the real variability of O₃ in the N.H. troposphere,

352 and, the increase in the observed concentrations and in the variability may likely indicate a
353 photochemical production of O₃ associated with anthropogenic precursor emissions (e.g. Logan
354 et al., 1985; Fusco and Logan, 2003; Dufour et al., 2010; Cooper et al., 2010; Wilson, et al.,
355 2012; Safieddine et al., 2013). Changes in biomass and biogenic emissions of NO_x, CO and non-
356 methane organic volatile compounds (NMVOC) may also play a role. However, they only
357 represent a small part of the total emissions for NO_x and CO (e.g. ~23% vs 72% for the
358 anthropogenic NO_x emissions and ~40% vs 60% for the anthropogenic CO emissions from the
359 emissions dataset used in the Supplement), while the biogenic emissions of NMVOC represent
360 the largest contribution to the total (~80%).

361
362 The zonal representation of the O₃ variability seen by IASI is given in Fig. 6. It shows the daily
363 number density at altitude levels corresponding to maximum of sensitivity in the four analyzed
364 layers in most of the cases (600 hPa - ~6km; 240 hPa - ~10km; 80 hPa - ~20km; 6 hPa - ~35
365 km) (Section 2). The top panel (~35 km) reflects well the photochemical O₃ production by
366 sunlight with the highest values in the equatorial belt during the summer (~3x10¹²
367 molecules/cm³). The middle panels (~20 km and ~10 km) shows the transport of ozone rich-air
368 to high latitudes in late winter (up to ~6x10¹² molecules/cm³ in the N.H.) which is induced by the
369 Brewer-Dobson circulation. The fact that the patterns at ~10km are similar to those at ~20 km
370 mainly reflects the low sensitivity of IASI to that level compared to the others. Finally, the lower
371 panel (~6 km) presents high O₃ levels in spring at high latitudes (~1.4x10¹² molecules/cm³ in the
372 N.H.), which likely reflects both the STE processes and the contribution from the stratosphere
373 due to the medium IASI sensitivity to that layer (see Section 2 and Supporting Information), and
374 a shift from high to middle latitudes in summer which could be attributed to anthropogenic O₃
375 production. The MLT panel also reflects the seasonal oscillation of the Inter-Tropical
376 Convergence Zone (ITCZ) around the Equator and the large fire activity in spring around 20°S-
377 40°S.

378 379 **4.2 Multivariate regression results: Seasonal and explanatory variables**

380 Figure 4(a) shows superimposed on the time series of the IASI ozone concentration profile, those
381 of the partial columns (dots) for the 4 layers (color contours). The adjusted daily time series to

382 these columns with the regression model defined by Eq.1 is also overlaid and shown by colored
383 lines. The model represents reasonably well the ozone variations in the four layers, with, as
384 illustrated for three latitude bands, good coefficient correlations (e.g. $R_{MLT}=0.94$; $R_{UTLS}=0.91$;
385 $R_{MLT}=0.90$ and $R_{US}=0.91$ for the 30°N-50°N band) and low residuals (< 8%) in all cases. The
386 regression model explains a large fraction of the variance in the daily IASI data over the
387 troposphere (~85%-95%) and the stratosphere (~85%-95% in all cases, except for the UST with
388 ~70-95%), as estimated from $\frac{\sigma(O_3^{Fitted_model}(t))}{\sigma(O_3(t))}$ where σ is the standard deviation relative to the
389 fitted regression model and to the IASI O₃ time series.

390
391 However, note that the fit fails to reproduce the highest ozone values ($>5 \times 10^{12}$ molecules/cm³)
392 above the seasonal maxima for 30°N-50°N latitude band, especially in the MLST during the
393 springs 2009 and 2010. This could be associated with occasional downward transport of upper
394 atmospheric NO_x-rich air occurring in winter and spring at high latitudes (Brohede et al., 2008)
395 following the strong subsidence within the intense Arctic vortex in 2009-2010 (Pitts et al., 2011)
396 or with the missing time-lags in the regression model between the QBO and ENSO variables and
397 the response of mid-latitude lower stratospheric ozone (Neu et al., 2014).

398
399 Fig.7 displays the annual cycle averaged over the 6 years recorded by IASI (dots) for the studied
400 layers and bands, as well as that from the fit of the daily O₃ columns (lines). The regression
401 model follows perfectly the O₃ variations in terms of timing of O₃ maxima and of amplitude of
402 the cycle. The fit is generally characterized by low residuals (<10%) and good correlation
403 coefficients (0.70-0.95), which indicates that the regression model is suitable to describe the
404 zonal variations. Exception is found over the Southern latitudes (residual up to 15% and R down
405 to 0.61) probably because of the variation induced by the ozone hole formation which is not
406 parameterized in the regression model, and because of the low temporal sampling of daytime
407 IASI measurements in this region.

408
409 From Figure 7, the following general patterns in the O₃ seasonal cycle can be isolated from the
410 zonally averaged IASI datasets:

- 411 1- In UST (top left panel), the maxima is in the equatorial belt, around 4.7×10^{18} molecules/cm²
412 throughout the year and the amplitudes are small compared to the averaged O₃ values. The
413 largest amplitude in the annual cycle is found in the N.H. between 30N and 50N where O₃
414 peaks in July after the highest solar elevation (in June) following a progressive buildup
415 during spring-summer. In agreement with FTIR observations (e.g. Steinbrecht et al., 2006;
416 Vigouroux et al., 2008), a shift of the O₃ maximum from spring (March-April) to late
417 summer (August-September) is found as one moves from high to low latitudes in the N.H. In
418 the S.H., the general shape of the annual cycle which shows a peak in October-November
419 before the highest solar elevation (in December), results from loss mechanisms depending on
420 annual cycle of temperatures and other trace gases. Other effects such as changing Brewer-
421 Dobson circulation, light absorption and tropical stratopause oscillations may also
422 considerably impact the cycle in this layer (Brasseur and Solomon, 1984; Schneider et al.,
423 2005).
- 424 2- In the lower stratosphere (MLST and UTLS, top right and bottom left panels), the
425 pronounced amplitudes of the annual cycle is dominated by the influence of the Brewer
426 Dobson circulation with the highest O₃ values observed over polar regions (reaching $\sim 6 \times 10^{18}$
427 molecules/cm² on average vs $\sim 2 \times 10^{18}$ molecules/cm² on average in the equatorial belt). The
428 maximum is shifted from late winter at high latitudes to spring at lower latitudes.
- 429 3- In MLT (bottom right panel), we clearly see a large hemispheric difference with the highest
430 values over the N.H. (also in UTLS). Maxima are observed in spring, reflecting more
431 effective STE processes. A particularly broad maximum from spring to late summer is
432 observed in the 30N-50N band. It probably points to anthropogenic production of O₃. This
433 has been further investigated in the Supplement through MOZART4-IASI comparison by
434 using constant anthropogenic emissions in the model settings (see Fig. S2). The results show
435 clear differences between the modeled and the observed MLT seasonal cycles, which
436 highlights the need for further investigation of the role of anthropogenically produced O₃ and
437 the realism of anthropogenic emissions inventories.

438
439 Figure 8 presents all the fitted regression parameters included in Eq. 1 (Section 3) in the four
440 layers as a function of latitude. The uncertainty in the 95% confidence limits which accounts for

441 the autocorrelation in the noise residual is given by error bars. The constant term (Fig.8a) is
 442 found to be statistically significant (uncertainty<10%) in all cases. It captures the two ozone
 443 maxima in the stratosphere: one over the Northern Polar regions in the MLST and one at
 444 equatorial latitudes in the UST ($\sim 4.5 \times 10^{18}$ molecules/cm²), the important decrease of O₃ in the
 445 lower stratospheric layers (UTLS and MLST) moving from high to equatorial latitudes, and the
 446 weak negative and strong positive gradients in the Northern MLT and in the UST, respectively.
 447 The sum of the constant terms of the four layers varies between 7.50×10^{18} (equatorial region) and
 448 9.50×10^{18} molecules/cm² (polar regions) and is similar to the one of the fitted total column
 449 (relative differences < 3.5%) (red line). Note that the constant terms in the UTLS region in the
 450 mid-latitudes and in the tropics are certainly affected by the fact that the FORLI-O₃ profiles are
 451 biased high by ~10-15% in this layer and latitude bands (Dufour et al., 2012; Gazeaux et al.,
 452 2012). The representativeness of the 20-degree zonal averages in terms of spatial variability has
 453 been examined by fitting the IASI time series for specific locations in the N.H. (results shown
 454 with stars in Fig.8a): the constant terms are found to be consistent, within their uncertainties,
 455 with those averaged per latitude bands in all cases. Over the polar region where O₃ shows a large
 456 natural variability, the regression coefficient is characterized by a large uncertainty.

457

458 The regression coefficients for other variables (harmonic and proxy terms) which are retained in
 459 the regression model by the stepwise elimination procedure are shown in Fig.8 (b). They are
 460 scaled by the fitted constant term and the error bars represent the uncertainty in the 95%
 461 confidence limits accounting for the autocorrelation in the noise residual. A positive (or
 462 negative) sign of the coefficients indicates that the associated variables are correlated (or anti-
 463 correlated) with the IASI O₃ time series. Note that if the uncertainty is larger than its associated
 464 estimate (i.e. larger than 100%, corresponding to an error bar overlapping the zero line), it means
 465 that the estimate becomes statistically non-significant when accounting for the autocorrelation in
 466 the noise residuals at the end of the elimination process. This is summarized in Table S1 of the
 467 Supplement. The contribution of the fitted variables into the IASI O₃ variations is estimated as

468
$$\frac{\sigma([a_n; b_n; x_j] [\cos(n\omega t); \sin(n\omega t); X_{norm,j}])}{\sigma(O_3(t))}$$
 where σ is the standard deviation relative to the fitted

469 signal of harmonic or proxy terms and to the IASI O₃ time series. From Figure 8, we find that:

470 1- The annual harmonic term (upper left) is the main driver of the O₃ variability and largely
471 dominates (scaled a_1+b_1 around $\pm 40\%$) over the semi-annual one (upper right; scaled a_2+b_2
472 around $\pm 15\%$). In UTLS and MLST, its amplitude decreases from high to low latitudes
473 likely following the cycle induced by the Brewer-Dobson circulation (*cfr.* Fig.6 and Fig.7)
474 and the sign of the coefficient accounts for the winter-spring maxima in both hemispheres
475 (negative values in the S.H. and positive ones in the N.H). The annual term contributes
476 importantly around 45%-85% of the observed O₃ variations, except in the 10°N-30°N and
477 equatorial bands (10%-30%), while the influence of the semi-annual variation on O₃ is
478 smaller (10%-25%) and highly variable between the bands. In the UST, the amplitudes vary
479 only slightly (around -5% to 5%) and account for the weak summer maximum. The
480 contributions of the annual harmonic term are estimated between 5%-30%. As expected, the
481 uncertainties associated with the annual terms are very weak and most of the harmonic terms
482 (annual and seasonal) are statistically significant.

483 2- The QBO and solar flux proxies are generally minor (scaled coefficients <10% and
484 contributions <15%) and they are often statistically non-significant contributors to O₃
485 variations after accounting for the autocorrelation in the noise residual (see Table S1 in the
486 Supplement), except in equatorial region (scaled coefficients of 10-15% in UTLS and
487 contributions up to 75% and 21% for QBO and SF, respectively) where they are important
488 drivers of O₃ variations (e.g. Logan et al., 2003; Steinbrecht et al., 2006b; Soukharev and
489 Hood, 2006; Fadnavis and Beig, 2009). Previous studies have indeed supported the solar
490 influence on the lower stratospheric equatorial dynamics (e.g. Soukharev and Hood, 2006;
491 McCormack et al., 2007). Note that the QBO³⁰ proxy (data not shown) has negative
492 coefficients for the mid-latitudes, which is in line with Frossard et al. (2013).

493 3- The contributions described by the ENSO and NAO/AAO proxies are generally very weak
494 (<10% and <5%, respectively), with scaled coefficients lower than 5%, and, in many cases
495 for the NAO/AAO proxies, they are even not statistically significant when taking into
496 account the correlation in the noise residuals (see Table S1 in Supplement). Despite of this, it
497 is worth pointing out that their effects to the O₃ variations are comparable to the results
498 published in the previous studies. The negative ENSO coefficient in the tropical UTLS is
499 consistent with results from Neu et al. (2014). Rieder et al. (2013) and Frossard et al. (2013)

500 have also shown large regions of negative coefficients for NAO North of 40°N, and large
501 regions of positive and negative coefficient estimates for ENSO, North of 30°N and South of
502 30°S, respectively.

503
504 We note that the non-representation of time-lags in the proxy time series may be underestimating
505 the role of some geophysical variables on O₃ variations, in particular that of ENSO and QBO in
506 zonal bands outside the regions where these geophysical quantities are measured (i.e. Niño
507 region 3.4 for ENSO and Singapore for QBO). Finally, we see in Fig.8 (b), large uncertainties
508 associated with the regression coefficients in UTLS in comparison with other layers, and in polar
509 regions in comparisons with other bands. We interpret this as an effect from the high natural
510 variability of O₃ measured by IASI in UTLS (see Fig.5) and from missing parameterizations and
511 low temporal sampling of daytime IASI measurements over the poles, respectively.

512
513 As a general feature, the results demonstrate the representativeness of the fitted models in each
514 layer and latitude band. This good performance of the regression procedure allows examination
515 of the adjusted linear trend term in Section 4.3 below.

516
517 **4.3 Multivariate regression results: trend over 2008-2013**

518 An additional goal of the multivariate regression method applied to the IASI O₃ time series is to
519 determine the linear trend term and its associated uncertainty. Despite the fact that more than 10
520 years of observations, corresponding to the large scale of solar cycle, is usually required to
521 perform such a trend analysis, we could argue that statistically relevant trends could possibly be
522 derived from the first six years of IASI observations, owing to the high spatio-temporal
523 frequency (daily) of IASI global observations, to the daily “fingerprint” in the solar flux (see
524 Figure 3 (a)), possibly making it distinguishable from a linear trend, and to its weak contribution
525 to O₃ variations (see section 4.2. and references therein). To verify the specific advantage of
526 IASI in terms of frequency sampling, we compare, in the subsections below, the statistical
527 relevance of the trends when retrieved from the monthly averaged IASI datasets *vs* the daily
528 averages as above, in the 20° zonal bands for the 4 partial and the total columns.

529

530 **4.3.1. Regressions applied on daily vs monthly averages**

531 Figure 9 (top) provides, as an example, the 6-year time series of IASI O₃ daily averages (left
532 panels) compared to the monthly averages (right panels) for the 30°S-50°S latitude band in the
533 UST (dark blue), along with the results from the regression procedure (light blue). Note that
534 either daily or monthly F10.7, NAO and AAO proxies (see Table 1) are used depending on the
535 frequency of the IASI O₃ averages to be adjusted. The second row in Fig.9 provides the
536 deseasonalised IASI and fitted time series, calculated by subtracting the model seasonal cycle
537 from the time series, as well as the residuals (red curves). The averaged residuals relative to the
538 deseasonalised IASI time series strongly vary with the layers and latitudinal bands and usually
539 range between 30% and 60%. The fitted signal in DU of each proxy is shown on the bottom
540 panels. The O₃ time series and the solar flux signal resulting from the adjustment without the
541 linear term trend in the regression model are also represented (orange lines in 2^d and bottom
542 panels, respectively). When it is not included in the regression model, the linear trend term is
543 only partly compensated by the solar flux term in the daily averages. This leads to an offset
544 between the fitted O₃ time series resulting from the both regression models (with and without the
545 linear term), which corresponds well to a trend over the IASI period, and, consequently, to larger
546 residuals (e.g. 80% without vs 44% with the linear term for this example and 94% without vs
547 58% with the linear term for the 30°S-50°S band in the MLST illustrated in Fig. S1 of the
548 Supplement). This offset is observed for a lot of layers and latitudinal bands. On the contrary, the
549 linear term can largely be compensated by the solar flux term in the monthly averages: the offset
550 is weak and the relative difference between the both fitted models is smaller (averaged
551 differences relative to the deseasonalised IASI time series of 10% in monthly data vs 17% in
552 daily data for this example). In this example, the linear and solar flux terms are even not
553 simultaneously retained in the iterative stepwise backward procedure when applied on the
554 monthly averages while they are when applied on daily averages. This effective co-linearity of
555 the linear and the monthly solar flux terms translates to larger model fit residuals (44% in daily
556 averages vs 60% in monthly averages in UST, relative to the deseasonalised IASI time series), to
557 smaller relative differences between both regression models (with and without the linear term)
558 (17% in daily vs 10% in monthly data), and to larger uncertainty on the trend coefficients when
559 using the monthly data in comparison with the daily data. This even leads, in this specific

560 example, to a not statistically significant linear term of $1.21 \pm 1.30 \text{ DU/yr}$ when derived from
561 monthly averages *vs* a significant trend of $1.74 \pm 0.77 \text{ DU/yr}$ from daily averages.

562
563 The same conclusions can be drawn from the fits in other layers and latitude bands, especially
564 those where the solar cycle variation of ozone is large (MLST and UTLs) or where the ozone
565 recovery occurs (UST). A larger trend uncertainty associated with monthly data *vs* daily data is
566 found in all situations (see Table 2, Section 4.3.2 below).

567
568 This brings us to the important conclusion that, thanks to the unprecedented sampling of IASI,
569 apparent trends can be detected in FORLI-O₃ time series even on a short period of
570 measurements. This supports the need for regular and high frequency measurements for
571 observing ozone variations underlined in other studies (e.g. Saunio et al., 2012). The O₃ trends
572 from the daily averages of IASI measurements are discussed and compared with results from the
573 monthly averages in the subsection below.

574

575 **4.3.2. O₃ trends from daily averages**

576 Table 2 summarizes the trends and their uncertainties in the 95% confidence limit, calculated for
577 each 20° zonal band and for the 4 partial and the total columns. In the northern and southern
578 polar regions, the polar night period is not covered because only IASI observations during
579 sunlight (over Feb-Oct and Oct-Apr for N.H. and S.H., respectively) are used in this study (See
580 Section 2). For the sake of comparison, the trends are reported for both the daily (top values) and
581 the monthly (bottom values) averages, and their uncertainties account for the auto-correlation in
582 the noise residuals considering a time lag of 1-day or 1-month, respectively. We show that the
583 daily and monthly trends in all layers and all latitude bands fall within each other uncertainties,
584 but that the use of daily median strongly helps in reducing everywhere the uncertainty associated
585 with the trends for the reasons discussed above (Section 4.3.1). This is particularly observed in
586 the UST where the ozone hole recovery would occur, but also in the MLST and the UTLs where
587 the solar cycle variation of ozone is the largest (see Figure 8). As a consequence, the UST trends
588 in monthly averages are shown to be mostly non-significant in comparison with those from daily

589 averages. Table 3 summarizes the trends in the daily averages for two 3-month periods: June-
590 July-August (JJA) and December-January-February (DJF).

591
592 From Tables 2 and 3, we observe very different trends according to the latitude and the altitude.
593 From Table 2, we find for the total columns that the trends derived from the daily medians are
594 only significant at high northern latitudes and that they are interestingly of the same order as
595 those obtained from other satellites and assimilated satellite data (Weatherhead and Anderson,
596 2006; Knibbe et al., 2014) or from ground-based measurements (Vigouroux et al., 2008)
597 calculated over longer time periods. The non-significant trends calculated for the mid- and low
598 latitudes of the N.H. are also comparable to the results published in the previous studies (Reinsel
599 et al., 2005; Andersen et al., 2006a; Vigouroux et al., 2008). Regarding the individual layers, we
600 find the following:

601 1- In the US, significant positive trends are observed in both hemispheres from the daily
602 medians, particularly over the mid- and high latitudes of both hemispheres (e.g. 1.74 ± 0.77
603 DU/yr in the 30°S-50°S band, i.e., 12%/decade) where the changes in ozone trends before
604 and after the turnaround in 1997 have been found to be the highest. Kyrola et al. (2013) and
605 Laine et al. (2014) report for instance a change of up to 10%/decade in O₃ trends between
606 1997-2011 vs 1984-1997. Positive trends in the UST are consistent with many previous
607 observations if one considers the fact that the period covered by IASI is later than those
608 reported in previous studies and that the recovery rate seems to increase since the beginning
609 of the turnaround (Knibbe et al. (2014) reports a factor of two increase in the recovery rate
610 between 1997-2010 with ~ 0.7 DU/yr and 2001-2010 with ~ 1.4 DU/yr in the S.H.). They could
611 indicate a leveling off of the negative trends that were observed since the second half of the
612 1990's mostly from satellites and ground-based monthly mean data (e.g. WMO 2006, 2011;
613 Randel and Wu, 2007; Vigouroux et al., 2008; Steinbrecht et al., 2009; Jones et al., 2009;
614 McLinden et al., 2009; Laine et al. 2014; Nair et al., 2014). The causes of this "turnaround"
615 remain, however, uncertain. If the compensating impact of decreasing chlorine in recent
616 years and maximum solar cycle (over 2011-2012 in the period studied here) is probably part
617 of the answer (e.g. Steinbrecht et al., 2004), the effects of changing stratospheric
618 temperatures and Brewer-Dobson circulation (Salby et al., 2002; Reinsel et al., 2005;

619 Dhomse et al., 2006; Manney et al., 2006) could also contribute and should be further
620 investigated. The long-lasting cold winter/spring 2011 in the Arctic leading to unprecedented
621 ozone loss (Manney et al., 2011), could explain the non-significant trend in the 70°N-90°N
622 band. This is supported by the results in winter (Table 3). From Table 3, we generally find
623 significant positive trends in summer N.H. and weaker positive or even non-significant trends
624 in winter S.H. A non-significant trend is also calculated for the 70°S-90°S band in spring
625 (data not shown). This could indicate the strong influence of changing stratospheric
626 temperatures on ozone depletion from year to year (e.g. Dhomse et al., 2006), leading to
627 larger uncertainties in our trends estimations and larger fitting residuals (see Section 4.2) due
628 to the fact that the stratospheric temperature is not taken into account as an explanatory
629 variable in the model.

630 2- In the MLST, one can see that, except in the high latitude bands, the trends are either non-
631 significant or significantly negative. This is in agreement with the trend analysis of Jones et
632 al. (2009) for the 20-25 km altitude range over the 1997-2008 period, as well as with other
633 studies at N.H. latitudes, which investigated O₃ changes in the 18-25 km range between 1996
634 and 2005 (Miller et al., 2006; Yang et al., 2006; Kivi et al., 2007). The results derived
635 separately for summer and winter in Table 3 are also in line with those of Kivi et al. (2007)
636 which reported contrasted trends in the Arctic MLST depending on season.

637 3- In the UTLS, negative trends are calculated in the tropics and significant positive trends are
638 found in the mid- and high latitudes of N.H., these latter falling within the uncertainties of
639 those reported by Kivi et al. (2007) for the tropopause-150 hPa layer between 1996 and 2003.
640 The large positive trends calculated at Northern latitudes (e.g. 1.28 ± 0.82 DU/year in the
641 70°N-90°N band) contribute for ~ 30 % to the positive trend for the total column. This result
642 is consistent with Yang et al. (2006) which reported that UTLS contributes 50% to positive
643 trends for the total columns measured in the mid-latitudes of the N.H. from ozonesondes. In
644 that study, these positive trends were linked to changes in atmospheric dynamics either
645 related to natural variability induced by potential vorticity and tropopause height variations
646 or related to anthropogenic climate change. Hence, the apparent increase in total ozone in the
647 mid-latitudes of the N.H. seen by IASI would reflect the combined contribution of dynamical
648 variability and declining ozone-depleting substances (e.g. Weatherhead and Andersen, 2006;

649 WMO, 2006; Harris et al., 2008, Nair et al., 2014). It is worth to keep in mind that these
650 effects are not independently accounted for in the regression model. Previous studies
651 reported, however, that dynamical and chemical processes are physically coupled in the
652 atmosphere, making difficult to define unambiguously such drivers in a statistical model (e.g.
653 Mäder et al., 2007; Harris et al., 2008). On a seasonal basis (see Table 3), the trends seen by
654 IASI at Northern latitudes in summer are all significantly positive and increasing towards the
655 pole. Note that the trends in upper layers may contribute to the ones calculated in UTLS due
656 to the medium IASI sensitivity to that layer (*cf.* Section 2).

657 4- In the MLT, most of the trends are significantly negative (Tables 2 and 3). The non-
658 significant trends in polar regions could be partly related to the lack of IASI sensitivity to
659 tropospheric O₃ (see Section 2, Fig.2). On a seasonal basis, we see that the negative trends
660 are more pronounced during the JJA period (around $-0.25 \pm 0.10 \text{ DU/yr}$) for all bands except
661 between 30°N and 10°S. In the N.H., these results tend to confirm the leveling off of
662 tropospheric ozone observed in recent years during the summer months (Logan et al., 2012).
663 This trend, however, remains difficult to interpret because it could be linked to a variety of
664 processes including most importantly: the decline of anthropogenic emissions of ozone
665 precursors, the increase of UV-induced O₃ destruction in the troposphere and STE processes
666 (Isaksen et al., 2005; Logan et al., 2012; Parrish et al., 2012; Hess and Zbinden, 2013). As a
667 consequence, it is hard to reconcile the trends in tropospheric ozone with changes in
668 emissions of ozone precursors. However, trends in emissions have already been able to
669 qualitatively explain measured ozone trends over some regions but with inconsistent
670 magnitude between observations and model simulations (e.g. Cooper et al., 2010; Logan et
671 al., 2012; Wilson et al., 2012). It is also worth to keep in mind that due to medium sensitivity
672 of IASI to the troposphere, the a priori contribution and ozone variations in stratospheric
673 layers may largely influence the trends seen by IASI in the MLT layer (*cf.* Section 2 and
674 Supporting Information).

675

676 **4.3.3. O₃ trends from IASI vs FTIR data**

677 In order to validate the trends inferred from IASI in the UST and in the total columns, we
678 compare them with those obtained from ground-based FTIR measurements at several NDACC

679 stations (Network for the Detection of Atmospheric Composition Change, available at
680 http://www.ndsc.ncep.noaa.gov/data/data_tbl/) by using the same fitting procedure and taking
681 into account the autocorrelation in the noise residuals. A box of $1^\circ \times 1^\circ$ centered on the stations
682 has been used for the collocation criterion. The regression model is applied on the daily FTIR
683 data for a series of time periods starting after the turnaround point (from 1998 for mid-latitude
684 stations and from 2000 for polar stations), as well as for the same periods as recently studied in
685 Vigouroux et al. (2014) for the sake of comparison. Note that because we are not interested here
686 in validating the IASI columns which was achieved in previous papers (e.g. Dufour et al., 2014;
687 Oetjen et al., 2014) but in validating the trends obtained from IASI, we did not correct biases
688 between IASI and FTIR due to different vertical sensitivity and *a priori* information. The results
689 are given in DU/year in Table 4. We see large significant positive total column trends from IASI
690 at middle and polar stations (e.g. 5.26 ± 4.72 DU/yr at Ny-Alesund), especially during spring.
691 These values are consistent with those reported in Knibbe et al. (2014) for the 2001-2010 period
692 in spring in the Antarctic (around 3-5DU/yr). This trend is not obtained from the FTIR data for
693 which trends are found to be mostly non-significant (even not retained in the stepwise
694 elimination procedure in some cases) as reported in Vigouroux et al. (2014), except at
695 Jungfraujoch which shows a trend of 5.28 ± 4.82 DU/yr over the 2008–2012 period. For the
696 periods starting before 2000, we calculated from FTIR, in agreement with Vigouroux et al.
697 (2014), a significantly negative trend at Ny-Alesund for the total column and significantly
698 positive trends at polar stations for the US. In addition, we see from Table 4 a leveling off of O_3
699 at polar stations in the UST after 2003, as previously reported in Vigouroux et al. (2014), which
700 was explained by a compensation effect between the decrease of solar cycle after its maximum in
701 2001-2002 and a positive trend. These trends are, however, non-significant and inferred only
702 from few FTIR measurements (see Number of days column, Table 4).

703

704 From IASI, it is worth to point out that, in all cases, positive trends are calculated in the UST
705 (even if some are not significant) and that these trends are consistent with those calculated from
706 FTIR data covering a ~ 11 -year period and starting after the turnaround (e.g. at Thule;
707 1.24 ± 1.09 DU/yr from IASI for the period 2008-2013 vs 1.42 ± 0.78 DU/yr from the FTIR over
708 2001-2012). This is illustrated for three stations (Ny-Alesund, Thule and Kiruna) in Fig.10 which

709 compares the time series from IASI (2008-2013, in red) with those from FTIR covering periods
710 starting after the turnaround (in blue). Their associated trends as well as the trend calculated from
711 FTIR covering the IASI period (in green) are also indicated.

712
713 In order to better characterize the effect of the temporal frequency on determining statistical
714 trends, the IASI time series have been subsampled to match the temporal resolution of FTIR. The
715 associated trend values are also indicated in Table 4 (2^d row). In any cases, we observe that the
716 fitted trends inferred from both IASI and FTIR with the same temporal samplings are within the
717 uncertainties of each other and that those associated with the subsampled IASI datasets are
718 significantly larger than those obtained with the daily ones, leading to statistically non-
719 significant trends.

720
721 Even if validating the IASI fitted trends with independent datasets is challenging due to the
722 short-time period of available IASI measurements and the insufficient number of usable
723 correlative measurements over such a short period, the results obtained for IASI vs FTIR tend to
724 confirm the conclusion drawn in subsections 4.3.1 and 4.3.2, that the high temporal sampling of
725 IASI provides good confidence in the determination of the trends even on periods shorter than
726 those usually required from other observational means.

727
728 **6 Summary and conclusions**

729 In this study, we have analyzed 6 years of IASI O₃ profile measurements as well as the total O₃
730 columns based on the profile. Four layers have been defined following the ability of IASI to
731 provide reasonably independent information on the ozone partial columns: the mid-lower
732 troposphere (MLT), the upper troposphere – lower stratosphere (UTLS), the mid-lower
733 stratosphere (MLST) and the upper stratosphere (UST). Based on daily values of these four
734 partial or of the total columns in 20-degree zonal averages, we have demonstrated the capability
735 of IASI for capturing large scale ozone variability (seasonal cycles and trends) in these different
736 layers. We have presented daytime vertical and latitudinal distributions for O₃ as well as their
737 evolution with time and we have examined the underlying dynamical or chemical processes. The
738 distributions were found to be controlled by photochemical production leading to a maximum in

739 summer at equatorial region in the UST, while they reflect the impact of the Brewer-Dobson
740 circulation with maximum in winter-spring at mid- and high latitude in the MLST and in the
741 troposphere. The effect of the photochemical production of O₃ from anthropogenic precursor
742 emissions was also observed in the troposphere with a shift in the timing of the maximum from
743 spring to summer in the mid-latitudes of the N.H.

744
745 The dynamical and chemical contributions contained in the daily time development of IASI O₃
746 have been analyzed by fitting the time series in each layer and for the total column with a set of
747 parameterized geophysical variables, a constant factor and a linear trend term. The model was
748 shown to perform well in term of residuals (<10%), correlation coefficients (between 0.70 and
749 0.99) and statistical uncertainties (<7%) for each fitted proxies. The annual harmonic terms
750 (seasonal behavior) were found to be largely dominant in all layers but the US, with fitted
751 amplitudes decreasing from high to low latitudes in agreement with the Brewer-Dobson
752 circulation. The QBO and solar flux terms were calculated to be important only in the equatorial
753 region, while other dynamical proxies accounted for in the regression (ENSO, NAO, AAO) were
754 found negligible.

755
756 Despite the short time period of available IASI dataset used in this study (2008-2013) and the
757 potential ambiguity between the solar and the linear trend terms, statistically significant trends
758 were derived from the six first years of daily O₃ partial columns measurements (on the contrary
759 to monthly averages which lead to mostly non-significant trends). This result which was
760 strengthened from comparisons with the regression applied on local FTIR measurements, is
761 remarkable as it demonstrates the added value of IASI exceptional frequency sampling for
762 monitoring medium to long-term changes in global ozone concentrations. We found two
763 important apparent trends:

764 1) Significant positive trends in the upper stratosphere, especially at high latitudes in both
765 hemispheres (e.g. 1.74 ± 0.77 DU/yr in the 30°S-50°S band), which are consistent with a probable
766 “turnaround” for upper stratospheric O₃ recovery (even if the causes of such a turnaround are
767 still under investigations). In addition, the trends calculated for some local stations are in line
768 with those calculated from FTIR measurements after the turnaround.

769 2) Negative trends in the troposphere at mid- and high Northern latitudes, especially during
770 summer (e.g. -0.26 ± 0.11 DU/yr in the 30°N-50°N band) which are in line with the decline of
771 ozone precursor emissions.

772

773 To confirm the above findings beyond the 6 first years of IASI measurements and to better
774 disentangle the effects of dynamical changes, of the 11-year solar cycle and of the equivalent
775 effective stratospheric chlorine (EESC) decline on the O₃ time series, further years of IASI
776 observations will be required, and more complete fitting procedures (including, among others,
777 proxies to account for the decadal trend in the EESC, for the ozone hole formation, for changes
778 in the Brewer-Dobson circulation, as well as including time lags in ENSO and QBO proxies) will
779 have to be explored. Further investigation on the regressors uncertainties and on the total error on
780 ozone measurements should be performed as well to understand on the unexplained variations in
781 IASI O₃ records.

782

783 This will be achievable with the long-term homogeneous records obtained by merging
784 measurements from the three successive IASI instruments on MetOp-A (2006); -B (2012) and –
785 C (2018), and by IASI successor on EPS-SG after 2021 (Clerbaux and Crevoisier, 2013;
786 Crevoisier et al., 2014).

787

788

789

790 **Acknowledgments**

791 IASI has been developed and built under the responsibility of the Centre National d'Etudes
792 Spatiales (CNES, France). It is flown onboard the MetOp satellites as part of the EUMETSAT
793 Polar System. The IASI L1 data are received through the EUMETCast near real time data
794 distribution service. Ozone data used in this paper are freely available upon request to the
795 corresponding author. We acknowledge support from the O₃-CCI project funded by ESA and by
796 the O3M-SAF project funded by EUMETSAT. P.-F. Coheur and C. Wespes are, respectively,
797 Senior Research Associate and Postdoctoral Researcher with F.R.S.-FNRS. The research in
798 Belgium was also funded by the Belgian State Federal Office for Scientific, Technical and
799 Cultural Affairs and the European Space Agency (ESA Prodex IASI Flow and BO₃MSAF). The
800 National Center for Atmospheric Research is funded by the National Science
801 Foundation.

802

803 **References**

- 804 Andersen, S. B. and Knudsen, B. M.: The influence of polar vortex ozone depletion on NH mid-
805 latitude ozone trends in spring, *Atmos. Chem. Phys.*, 6, 2837–2845, 2006a.
- 806 Andersen, S. B., Weatherhead, E. C., Stevermer, A., Austin, J., Brühl, C., Fleming, E. L., de
807 Grandpré, J., Grewe, V., Isaksen, I., Pitari, G., Portmann, R. W., Rognerud, B., Rosenfield, J. E.,
808 Smyshlyaev, S., Nagashima, T., Velders, G. J. M., Weisenstein, D. K., and Xia, K.: Comparison
809 of recent modeled and observed trends in total column ozone, *J. Geophys. Res.*, 111, D02303,
810 doi:10.1029/2005JD006091, 2006b.
- 811 Anton, M., D. Loyola, C. Clerbaux, M. Lopez, J. Vilaplana, M. Banon, J. Hadji-Lazaro, P.
812 Valks, N. Hao, W. Zimmer, P. Coheur, D. Hurtmans, and L. Alados-Arboledas: Validation of the
813 Metop-A total ozone data from GOME-2 and IASI using reference ground-based measurements
814 at the Iberian peninsula, *Remote Sensing of Environment*, 115, 1380-1386, 2011.
- 815 August, T., D. Klaes, P. Schlüssel, T. Hultberg, M. Crapeau, A. Arriaga, A., O'Carroll, A.,
816 Coppens, D., Munro, R., Calbet, X.: IASI on Metop-A: Operational Level 2 retrievals after five
817 years in orbit. *Journal of Quantitative Spectroscopy and Radiative Transfer*, 114(11), 1340–1371,
818 2012.
- 819 Barret, B., Le Flochmoen, E., Sauvage, B., Pavelin, E., Matricardi, M., and Cammas, J. P.: The
820 detection of post-monsoon tropospheric ozone variability over south Asia using IASI data,
821 *Atmos. Chem. Phys.*, 11, 9533-9548, doi:10.5194/acp-11-9533-2011, 2011.
- 822 Bourassa, A. E., D. A. Degenstein, W. J. Randel, J. M. Zawodny, E. Kyrölä, C. A. McLinden, C.
823 E. Sioris, and C. Z. Roth: Trends in stratospheric ozone derived from merged SAGE II and Odin-
824 OSIRIS satellite observations, *Atmos. Chem. Phys.*, 14, 6983–6994, doi:10.5194/acp-14-6983-
825 2014, 2014.
- 826 Boynard, A., C. Clerbaux, P.-F. Coheur, D. Hurtmans, S. Turquety, M. George, J. Hadji-Lazaro,
827 C. Keim, and J. Meyer-Arnek: Measurements of total and tropospheric ozone from IASI:
828 comparison with correlative satellite, ground-based and ozonesonde observations, *Atmos. Chem.*
829 *Phys.*, 9, 6255-6271, 2009.
- 830 Brohede, S., McLinden, C. A., Urban, J., Haley, C. S., Jonsson, A. I., and Murtagh, D.: Odin
831 stratospheric proxy NO_y measurements and climatology, *Atmos. Chem. Phys.*, 8, 5731–5754,
832 doi:10.5194/acp-8-5731 2008, 2008.

833 Brasseur, G. and Solomon, S: *Aeronomy of the Middle Atmosphere*, 441 pp., D. Reidel
834 Publishing Company, Dordrecht, The Netherlands, 1984.

835 Chipperfield, M. P., Kinnersley, J. S., and Zawodny, J.: A two-dimensional model study of the
836 QBO signal in SAGE II NO₂ and O₃, *Geophys. Res. Lett.*, 21, 589–592, 1994.

837 Chipperfield, M. P.: A three-dimensional model study of longterm mid-high latitude lower
838 stratosphere ozone changes, *Atmos. Chem. Phys.*, 3, 1253–1265, 2003.

839 Clarisse L., D. Hurtmans, C. Clerbaux, J. Hadji-Lazaro, Y. Ngadi, P.-F. Coheur: Retrieval of
840 sulphur dioxide from the infrared atmospheric sounding interferometer (IASI)
841 *Atmospheric Measurement Techniques* 5, 3, 581-594, 2012.

842 Clerbaux, C., A. Boynard, L. Clarisse, M. George, J. Hadji-Lazaro, H. Herbin, D. Hurtmans, M.
843 Pommier, A. Razavi, S. Turquety, C. Wespes, and P.-F. Coheur: Monitoring of atmospheric
844 composition using the thermal infrared IASI/MetOp sounder, *Atmos. Chem. Phys.*, 9, 6041-
845 6054, 2009.

846 Clerbaux C. and C. Crevoisier: New Directions: Infrared remote sensing of the troposphere from
847 satellite: Less, but better, *Atmospheric Environment*, 72, 24-26, 2013.

848 Coheur, P.-F., B. Barret, S. Turquety, D. Hurtmans, J. Hadji-Lazaro, and C. Clerbaux: Retrieval
849 and characterization of ozone vertical profiles from a thermal infrared nadir sounder, *J. Geophys.*
850 *Res.*, 110, D24, 303, doi:10.1029/2005JD005845, 2005.

851 Cooper, O., Parrish, D., Stohl, A., Trainer, M., Nédélec, P., Thouret, V., Cammas, J., Oltmans,
852 S., Johnson, B., and Tarasick, D.: Increasing springtime ozone mixing ratios in the free
853 troposphere over western North America, *Nature*, 463, 344–348, doi:10.1038/nature08708, 2010.

854 Crevoisier, C., Clerbaux, C., Guidard, V., Phulpin, T., Armante, R., Barret, B., Camy-Peyret, C.,
855 Chaboureaud, J.-P., Coheur, P.-F., Crépeau, L., Dufour, G., Labonnote, L., Lavanant, L., Hadji-
856 Lazaro, J., Herbin, H., Jacquinet-Husson, N., Payan, S., Péquignot, E., Pierangelo, C., Sellitto,
857 P., and Stubenrauch, C. : Towards IASI-New Generation (IASI-NG): impact of improved
858 spectral resolution and radiometric noise on the retrieval of thermodynamic, chemistry and
859 climate variables, *Atmos. Meas. Tech.*, 7, 4367–4385, 2014.

860 de Laat, A. T. J., R. J. van der A, and M. van Weele: Tracing the second stage of ozone recovery
861 in the Antarctic ozone-hole with a “big data” approach to multivariate regressions, *Atmos.*
862 *Chem. Phys.*, 15, 79–97, doi:10.5194/acp-15-79-2015, 2015.

863 Dhomse, S., Weber, M., Wohltmann, I., Rex, M., and Burrows, J. P.: On the possible causes of
864 recent increases in northern hemispheric total ozone from a statistical analysis of satellite data
865 from 1979 to 2003, *Atmos. Chem. Phys.*, 6, 1165–1180, doi:10.5194/acp-6-1165-2006, 2006.

866 Dufour, G., M. Eremenko, J. Orphal, and J.-M. Flaud: IASI observations of seasonal and day-to-
867 day variations of tropospheric ozone over three highly populated areas of China: Beijing,
868 Shanghai, and Hong Kong, *Atmos. Chem. Phys.*, 10, 3787–3801, 2010.

869 Dufour, G., M. Eremenko, A. Griesfeller, B. Barret, E. LeFlochmoen, C. Clerbaux, J. Hadji-
870 Lazaro, P.-F. Coheur, and D. Hurtmans: Validation of three different scientific ozone products
871 retrieved from IASI spectra using ozonesondes, *Atmos. Meas. Tech.*, 5, 611–630, 2012.

872 Fadnavis, S. and Beig, J.: Quasibiennial Oscillation in Ozone and Temperature over Tropics, *J.*
873 *Atmos. Sol. Terr. Phys.*, 71, 1450–1455, doi:10.1016/j.jastp.2008.11.012, 2009.

874 Gardiner, T., Forbes, A., de Mazière, M., Vigouroux, C., Mahieu, E., Demoulin, P., Velasco, V.,
875 Notholt, J., Blumenstock, T., Hase, F., Kramer, I., Sussmann, R., Stremme, W., Mellqvist, J.,
876 Strandberg, A., Ellingsen, K., and Gauss, M.: Trend analysis of greenhouse gases over Europe
877 measured by a network of ground-based remote FTIR instruments, *Atmos. Chem. Phys.*, 8,
878 6719–6727, 2008.

879 Frossard, L., H.E. Rieder, M. Ribatet, J. Staehelin, J. A. Maeder, S. Di Rocco, A. C. Davison, T.
880 Pete.: On the relationship between total ozone and atmospheric dynamics and chemistry at mid-
881 latitudes – Part 1: Statistical models and spatial fingerprints of atmospheric dynamics and
882 chemistry, *Atmos. Chem. Phys.*, 13, 147–164, doi:10.5194/acp-13-147-2013, 2013.

883 Fusco, A. C. and Logan, J. A., Analysis of 1970–1995 trends in tropospheric ozone at Northern
884 Hemisphere midlatitudes with the GEOS-CHEM model, *J. Geophys. Res.*, 108, 4449,
885 doi:10.1029/2002JD002742, 2003.

886 Gazeaux, J., C. Clerbaux, M. George, J. Hadji-Lazaro, J. Kuttippurath, P.-F. Coheur, D.
887 Hurtmans, T. Deshler, M. Kovilakam, P. Campbell, V. Guidard, F. Rabier, and J.-N. Thepaut:
888 Intercomparison of polar ozone profiles by IASI/Metop sounder with 2010 concordiasi
889 ozonesonde observations, *Atmos. Meas. Tech.*, 5, 7923–7944, 2012.

890 Hadjinicolaou, P., Pyle, J. A., and Harris, N. R. P.: The recent turnaround in stratospheric ozone
891 over northern middle latitudes: A dynamical modeling perspective, *Geophys. Res. Lett.*, 32,
892 L12821, doi:10.1029/2005GL022476, 2005.

893 Harris, N. R. P., E. Kyrö, J. Staehelin, D. Brunner, S.-B. Andersen, S. Godin-Beekmann, S.,
894 Dhomse, P. Hadjinicolaou, G. Hansen, I. Isaksen, A. Jrrar, A. Karpetchko, R. Kivi, B. Knudsen,
895 P. Krizan, J. Lastovicka, J. Maeder, Y. Orsolini, J. A. Pyle, M. Rex, K. Vanicek, M. Weber, I.
896 Wohltmann, P. Zanis and C. Zerefos: Ozone trends at northern mid- and high latitudes – a
897 European perspective. *Ann. Geophys.*, 26, 1207-1220, 2008.

898 Hauchecorne, A., Bertaux, J. L., Dalaudier, F., Keckhut, P., Lemennais, P., Bekki, S., Marchand,
899 M., Lebrun, J. C., Kyrölä, E., Tamminen, J., Sofieva, V., Fussen, D., Vanhellefont, F., Fanton
900 d’Andon, O., Barrot, G., Blanot, L., Fehr, T., and Saavedra de Miguel, L.: Response of tropical
901 stratospheric O₃, NO₂ and NO₃ to the equatorial Quasi-Biennial Oscillation and to temperature as
902 seen from GOMOS/ENVISAT, *Atmos. Chem. Phys. Discuss.*, 10, 9153–9171,
903 doi:10.5194/acpd-10-9153-2010, 2010.

904 Hess, P.G. and Zbinden, R.: Stratospheric impact on tropospheric ozone variability and trends:
905 1990–200, *Atmos. Chem. Phys.*, 13, 649–674, 2013.

906 Hofmann, D.J.: Recovery of Antarctic ozone hole, *Nature* 384, 222-223 doi:10.1038/384222a0,
907 1996.

908 Hood, L. L. and Soukharev, B. E.: Solar induced variations of odd nitrogen: Multiple regression
909 analysis of UARS HALOE data, *Geophys. Res. Lett.*, 33, L22805, doi:10.1029/2006GL028122,
910 2006.

911 Hurtmans, D., P. Coheur, C.Wespes, L. Clarisse, O. Scharf, C. Clerbaux, J. Hadji-Lazaro, M.
912 George, and S. Turquety: FORLI radiative transfer and retrieval code for IASI, *Journal of*
913 *Quantitative Spectroscopy and Radiative Transfer*, 113, 1391-1408, 2012.

914 Isaksen I. S. A., Zerefos, C. S., Kourtidis, K., Meleti, C., Dalsøren, S. B., Sundet, J. K., Grini, A.,
915 Zanis, P., and Balis, D.: Tropospheric ozone changes at unpolluted and semipolluted regions
916 induced by stratospheric ozone changes, *J. Geophys. Res.*, 110, D02302,
917 doi:10.1029/2004JD004618, 2005.

918 Jiang, X., Pawson, S., Camp, C. D., Nielsen, E., Shia, R., Liao, T., Jeev, K., Limpasuvan, V., and
919 Yung, Y. L.: Interannual variability and trends in extratropical ozone. Part II: Southern
920 Hemisphere, *J. Atmos. Sci.*, 65, 3030–3041, 2008.

921 Jones , A., J. Urban, D.P. Murtagh, P. Eriksson, S. Brohede, C. Haley, D. Degenstein, A.
922 Bourassa, C. von Savigny, T. Sonkaew, A. Rozanov, H. Bovensmann, and J. Burrows, *Evolution*

923 of stratospheric ozone and water vapour time series studied with satellite measurements, *Atmos.*
924 *Chem. Phys.*, 9 (16), 6055-6075, doi: 10.5194/acp-9-6055-2009, 2009.

925 Kuttippurath, J., F. Lefèvre, J.-P. Pommereau, H. K. Roscoe, F. Goutail, A. Pazmiño, and J. D.
926 Shanklin: Antarctic ozone loss in 1979–2010: First sign of ozone recovery, *Atmos. Chem.*
927 *Phys.*, 1625–1635, 2013.

928 Kuttippurath, J., G. E. Bodeker, H. K. Roscoe, and P. J. Nair: A cautionary note on the use of
929 EESC-based regression analysis for ozone trend studies, *Geophys. Res. Lett.*, 42, 162–168,
930 doi:10.1002/2014GL062142, 2015.

931 Kivi, R., Kyrö, E., Turunen, T., Harris, N. R. P., von der Gathen, P., Rex, M., Andersen, S. B.,
932 and Wohltmann, I.: Ozone observations in the Arctic during 1989-2003: Ozone variability
933 and trends in the lower stratosphere and free troposphere, *J. Geophys. Res.*, 112, D08306,
934 doi:10.1029/2006JD007271, 2007.

935 Knibbe J. S., R. J. van der A, and A. T. J. de Laat: Spatial regression analysis on 32 years of total
936 column ozone data, *Atmos. Chem. Phys.*, 14, 8461–8482, 2014.

937 Kramarova, N.A., E. R. Nash, P. A. Newman, P. K. Bhartia, R. D. McPeters, D. F. Rault, C. J.
938 Seftor, P. Q. Xu, and G. J. Labow: Measuring the Antarctic ozone hole with the new Ozone
939 Mapping and Profiler Suite (OMPS), *Atmos. Chem. Phys.*, 14, 2353–2361, 2014.

940 Kyrölä, E., Tamminen, J., Leppelmeier, G. W., Sofieva, V., Hassinen, S., Seppälä, A., Verronen,
941 P. T., Bertaux, J.-L., Hauchecorne, A., Dalaudier, F., Fussen, D., Vanhellemont, F., d’Andon, O.
942 F., Barrot, G., Mangin, A., Theodore, B., Guirlet, M., Koopman, R., Saavedra, L., Snoeij, P., and
943 Fehr, T.: Nighttime ozone profiles in the stratosphere and mesosphere by the Global Ozone
944 Monitoring by Occultation of Stars on Envisat, *J. Geophys. Res.*, 111, D24306,
945 doi:10.1029/2006JD007193, 2006.

946 Kyrölä, E.; Tamminen, J.; Sofieva, V.; Bertaux, J. L.; Hauchecorne, A.; Dalaudier, F.; Fussen,
947 D.; Vanhellemont, F.; Fanton d’Andon, O.; Barrot, G.; Guirlet, M.; Fehr, T. and Saavedra de
948 Miguel, L.: GOMOS O₃, NO₂, and NO₃ observations in 2002–2008, *Atmos. Chem. Phys.*, 10,
949 7723–7738, 2010, doi:10.5194/acp-10-7723-2010.

950 Kyrölä, E., Laine, M., Sofieva, V., Tukiainen, S., Tamminen, J., Päivärinta, S., Zawodny, J., and
951 Thomason, L.: Combined SAGE II-GOMOS ozone profile data set for 1984–2011 and trend

952 analysis of the vertical distribution of ozone, *Atmos. Chem. Phys.*, 13, 10645–10658,
953 doi:10.5194/acp-13-10645-2013, 2013.

954 Laine, M. , N. Latva-Pukkila, and E. Kyrölä: Analysing time-varying trends in stratospheric
955 ozone time series using the state space approach, *Atmos. Chem. Phys.*, 14, 9707–9725, 2014.

956 Logan, J. A.: Tropospheric Ozone: Seasonal behaviour, Trends, and Anthropogenic Influence, *J.*
957 *Geophys. Res.*, 90(D6), 10 463–10 482, 1985.

958 Logan, J. A., Jones, D. B. A., Megretskaia, I. A., Oltmans, S. J. Johnson, B. J., Vömel, H.,
959 Randel, W. J., Kimani, W., and Schmidlin, F. J.: Quasi-biennial oscillation in tropical ozone as
960 revealed by ozonesonde and satellite data, *J. Geophys. Res.*, 108(D8), 4244,
961 doi:10.1029/2002JD002170, 2003

962 Logan, J. A., Staehelin, J., Megretskaia, I. A., Cammas, J.-P. , Thouret, V., Claude, H., De
963 Backer, H., Steinbacher, M., Scheel, H.-E., Stübi, R., Fröhlich, M., and Derwent R.: Changes in
964 ozone over Europe: Analysis of ozone measurements from sondes, regular aircraft (MOZAIC)
965 and alpine surface sites, *J. Geophys. Res.*, 117, D09301, doi:10.1029/2011JD016952, 2012.

966 Mäder, J. A., Staehelin, J., Brunner, D., Stahel, W. A., Wohltmann, I., and Peter, T.: Statistical
967 modelling of total ozone: Selection of appropriate explanatory variables, *J. Geophys. Res.*, 112,
968 D11108, doi:10.1029/2006JD007694, 2007.

969 Mäder, J.A., J. Staehelin, T. Peter, D. Brunner, H. E. Rieder, and W. A. Stahel: Evidence for the
970 effectiveness of the Montreal Protocol to protect the ozone layer, *Atmos. Chem. Phys.*, 10,
971 12161-12171, 2010.

972 Manney, G. L., Santee, M. L., Froidevaux, L., Hoppel, K., Livesey, N. J., and Waters, J. W.:
973 EOS MLS observations of ozone loss in the 2004–2005 Arctic winter, *Geophys. Res. Lett.*, 33,
974 L04802, doi:10.1029/2005GL024494, 2006.

975 Manney, G. Santee, M. L., Rex, M., Livesey, N. J., Pitts, M.C., Veefkind, P., Nash, E. N.,
976 Wohltmann, I., Lehmann, R., Froidevaux, L., Poole, L. R., Schoeberl, M. R., Haffner, D.P.,
977 Davies, J., Dorokhov, V., Gernandt, H., Johnson, B., Kivi, R., Kyrö, E., Larsen, N., Levelt, P. F.,
978 Makshtas, A., McElroy, C. T., Nakajima, H., Parrondo, M.C., Tarasick, D. W., von der Gathen,
979 P., Walker, K. A., and Zinoviev, N. S. : Unprecedented Arctic ozone loss in 2011, *Nature*, 478,
980 469–475, doi:10.1038/nature10556, 2011.

981 McCormack, J.P., D.E. Siskind and L.L. Hood: Solar-QBO interaction and its impact on
982 stratospheric ozone in a zonally averaged photochemical transport model of the middle
983 atmosphere, *J. Geophys. Res.*, 112, D16109, doi:10.1029/2006JD008369, 2007.

984 McLinden, C.A., S. Tegtmeier, and V. Fioletov, Technical note: A SAGE-corrected SBUV
985 zonal-mean ozone data set, *Atmos. Chem. Phys.*, 9 (20), 7963-7972, doi: 10.5194/acp-9-7963-
986 2009, 2009.

987 McPeters, R. D., Labow, G. J., and Logan, J. A.: Ozone climatological profiles for satellite
988 retrieval algorithms, *J. Geophys. Res.-Atmos.*, 112, D05308, doi:10.1029/2005JD006823, 2007.

989 Miller, A. J., Cai, A., Tiao, G., Wuebbles, D. J., Flynn, L. E., Yang, S.-K., Weatherhead, E. C.,
990 Fioletov, V., Petropavlovskikh, I., Meng, X.-L., Guillas, S., Nagatani, R. M., and Reinsel, G. C.:
991 Examination of ozonesonde data for trends and trend changes incorporating solar and Arctic
992 oscillation signals, *J. Geophys. Res.*, 111, D13305, doi:10.1029/2005JD006684, 2006.

993 Nair, P. J., S. Godin-Beekmann, J. Kuttippurath, G. Ancellet, F. Goutail, A. Pazmiño, L.
994 Froidevaux, J. M. Zawodny, R. D. Evans, H. J. Wang, J. Anderson, and M. Pastel: Ozone trends
995 derived from the total column and vertical profiles at a northern mid-latitude station, *Atmos.*
996 *Chem. Phys.*, 13, 10373–10384, 2013.

997 Neu, J.L., T. Flury, G. L. Manney, M. L. Santee, N. J. Livesey and J. Worden, Tropospheric
998 ozone variations governed by changes in stratospheric circulation, *Nat. Geosc.*, 7, 340–344,
999 doi:10.1038/ngeo2138, 2014.

1000 Newchurch, M.J., Yang, E.-S., Cunnold, D.M., Reinsel, G.C. and Zawodny, J.M.: Evidence for
1001 slowdown in stratospheric ozone loss: first stage of ozone recovery, *J. Geophys. Res. Atmos.*,
1002 108, D16, doi:10.1029/2003JD003471, 2003.

1003 Oetjen, H., Payne, V.H., Kulawik, S.S., Eldering, A., Worden, J., Edwards, D.P., Francis, G.L.,
1004 Worden, H.M., Clerbaux, C., Hadji-Lazaro, J., Hurtmans, D. : Extending the satellite data record
1005 of tropospheric ozone profiles from Aura-TES to MetOp-IASI, *Atmos. Meas. Tech. Discuss.*, 7,
1006 7013–7051, 2014.

1007 Oltmans, S. J., Lefohn, A. S., Scheel, H. E., Harris, J. M., Levy II., H., Galbally, I. E., Brunke,
1008 E., Meyer, C. P., Lathrop, J. A., Johnson, B. J., Shadwick, D. S., Cuevas, E., Schmidlin, F. J.,
1009 Tarasick, D.W., Claude, H., Kerr, J. B., Uchino, O., and Mohnen, V.: Trends of ozone in the
1010 troposphere, *Geophys. Res. Lett.*, 25, 139–142, doi:10.1029/97GL03505, 1998.

1011 Oltmans, S. J., Lefohn, A. S., Harris, J. M., Galbally, I., Scheel, H. E., Bodeker, G., Brunke, E.,
1012 Claude, H., Tarasick, D., Johnson, B. J., Simmonds, P., Shadwick, D., Anlauf, K., Hayden, K.,
1013 Schmidlin, F., Fujimoto, T., Akagi, K., Meyer, C., Nichol, S., Davies, J., Redondas, A., and
1014 Cuevas, E.: Long-term changes in tropospheric ozone, *Atmos. Environ.*, 40, 3156–3173, 2006.

1015 Parrington, M., P. I. Palmer, D. K. Henze, D. W. Tarasick, E. J. Hyer, R. C. Owen, D. Helmig,
1016 C. Clerbaux, K. W. Bowman, M. N. Deeter, E. M. Barratt, P.-F. Coheur, D. Hurtmans, Z. Jiang,
1017 M. George, and J. R. Worden: The influence of boreal biomass burning emissions on the
1018 distribution of tropospheric ozone over north America and the north Atlantic during 2010,
1019 *Atmos. Chem. Phys.*, 12, 2077-2098, doi: 10.5194/acp-12-2077-2012, 2012.

1020 Parrish, D.D., K. S. Law, J. Staehelin, R. Derwent, O. R. Cooper,¹ H. Tanimoto, A. Volz
1021 Thomas, S. Gilge, H.-E. Scheel, M. Steinbacher, and E. Chan: Long-term changes in lower
1022 tropospheric baseline ozone concentrations at northern mid-latitudes, *Atmos. Chem. Phys.*, 12,
1023 11485–11504, 2012.

1024 Pitts, M. C., Poole, L. R., Dörnbrack, A., and Thomason, L. W.: The 2009–2010 Arctic polar
1025 stratospheric cloud season: a CALIPSO perspective, *Atmos. Chem. Phys.*, 11, 2161–2177,
1026 doi:10.5194/acp-11-2161-2011, 2011.

1027 Pommier, M., C. Clerbaux, K. S. Law, G. Ancellet, P. Bernath, P.-F. Coheur, J. Hadji- Lazaro,
1028 D. Hurtmans, P. Nedelec, J.-D. Paris, F. Ravetta, T. B. Ryerson, H. Schlager, and A.
1029 J. Weinheimer: Analysis of IASI tropospheric O₃ data over the arctic during POLARCAT
1030 campaigns in 2008, *Atmos. Chem. Phys.*, 12, 7371-7389, doi:doi:10.5194/acp-12-7371-2012,
1031 2012.

1032 Randel, W. J. and Wu, F.: Isolation of the ozone QBO in SAGE II data by singular-value
1033 decomposition, *J. Atmos. Sci.*, 53, 2546– 2559, 1996.

1034 Randel, W. J. and Wu, F.: A stratospheric ozone profile data set for 1979-2005: Variability,
1035 trends, and comparisons with column ozone data, *J. Geophys. Res.-Atmos.*, 112, D06313,
1036 doi:10.1029/ 2006JD007339, 2007.

1037 Reinsel, G. C., Weatherhead, E. C. , Tiao, G. C., Miller, A. J., Nagatani, R. M., Wuebbles, D. J.,
1038 and Flynn, L. E.: On detection of turnaround and recovery in trend for ozone, *J. Geophys. Res.*,
1039 107, D10, doi:10.1029/2001JD000500, 2002.

1040 Reinsel, G. C., Miller, A. J., Weatherhead, E. C., Flynn, L. E., Nagatani, R. M., Tiao, G. C., and
1041 Wuebbles, D. J.: Trend analysis of total ozone data for turnaround and dynamical contributions,
1042 *J. Geophys. Res.*, 110, D16306, doi:10.1029/2004JD004662, 2005.

1043 Rodgers, C. D.: Inverse methods for atmospheric sounding: Theory and Practice, Series on
1044 Atmospheric, Oceanic and Planetary Physics, Vol. 2, World Scientific Publishing Co.,
1045 Singapore, 2000.

1046 Rieder, H. E., Frossard, L., Ribatet, M., Staehelin, J., Maeder, J. A., Di Rocco, S., Davison, A.
1047 C., Peter, T., Weihs, P., and Holawe, F.: On the relationship between total ozone and atmospheric
1048 dynamics and chemistry at mid-latitudes – Part 2: The effects of the El Nino/Southern
1049 Oscillation, volcanic eruptions and contributions of atmospheric dynamics and chemistry to
1050 long-term total ozone changes, *Atmos. Chem. Phys.*, 13, 165–179, doi:10.5194/acp-13- 165-
1051 2013, 2013.

1052 Safieddine S., Clerbaux C., George M., Hadji-Lazaro J., Hurtmans D., Coheur P.-F., Wespes C.,
1053 Loyola D., Valks P., Hao N.: Tropospheric ozone and nitrogen dioxide measurements in urban
1054 and rural regions as seen by IASI and GOME-2, *J. Geophys. Res.*, 118, 18, 10555-10566, 2013.

1055 Salby, M., P. Callaghan, P. Keckhut, S. Godin, and M. Guirlet: Interannual changes of
1056 temperature and ozone: Relationship between the lower and upper stratosphere, *J. Geophys.*
1057 *Res.*, 107(D18), 4342, doi:10.1029/2001JD000421, 2002.

1058 Salby, M., Titova, E., and Deschamps, L.: Rebound of Antarctic ozone, *Geophys. Res. Lett.*, 38,
1059 L09702, doi:10.1029/2011GL047266, 2011.

1060 Santer, B.D., Wigley, T.M.L., Boyle, J.S., Gaffen, D.J., Hnilo, J.J., Nychka, D., Parker, D.E.,
1061 Parker, D.E. and Taylor, K.E.: Statistical significance of trends and trend differences in layer-
1062 average atmospheric temperature time series, *J. Geophys. Res.*, 105(D6), 7337-7356, 2000.

1063 Saunio, M., Emmons, L., Lamarque, J.-F., Tilmes, S., Wespes, C., Thouret, V., and Schultz, M.:
1064 Impact of sampling frequency in the analysis of tropospheric ozone observations, *Atmos. Chem.*
1065 *Phys.*, 12, 6757–6773, doi:10.5194/acp-12-6757-2012, 2012.

1066 Scannell, C., D. Hurtmans, A. Boynard, J. Hadji-Lazaro, M. George, A. Delcloo, A. Tuinder,
1067 P.F. Coheur, and C. Clerbaux: Antarctic ozone hole as observed by IASI/MetOp for 2008-2010,
1068 *Atmos. Meas. Tech.*, 5, 123-139, 2012.

1069 Schneider, M., Blumenstock, T., Hase, F., Höpfner, M., Cuevas, E., Redondas, A., and Sancho,
1070 J. M.: Ozone profiles and total column amounts derived at Izana Tenerife Island, from FTIR
1071 solar absorption spectra, and its validation by an intercomparison to ECC-sonde and Brewer
1072 spectrometer measurements, *J. Quant. Spectros. Radiat. Transfer*, 91, 3, 245–274,
1073 doi:10.1016/j.jqsrt.2004.05.067, 2005.

1074 Shepherd, T.G., D. A. Plummer, J. F. Scinocca, M. I. Hegglin, V. E. Fioletov, M. C. Reader, E.
1075 Remsberg, T. von Clarmann, H. J. Wang: Reconciliation of halogen-induced ozone loss with the
1076 total-column ozone record, *Nature Geoscience*, 7, 443–449, doi:10.1038/ngeo2155, 2014.

1077 Soukharev, B. E. and Hood, L. L.: Solar cycle variation of stratospheric ozone: Multiple
1078 regression analysis of long-term satellite data sets and comparisons with models, *J. Geophys.*
1079 *Res.- Atmos.*, 111, D20314, doi:10.1029/2006JD007107, 2006.

1080 Steinbrecht, W., Claude, H., and Winkler, P.: Enhanced upper stratospheric ozone: Sign of
1081 recovery or solar cycle effect?, *J. Geophys. Res.*, 109, D02308, doi:10.1029/2003JD004284,
1082 2004.

1083 Steinbrecht, W., Claude, H., Schonenborn, F., McDermid, I. S., Leblanc, T., Godin, S., Song, T.,
1084 Swart, D. P. J., Meijer, Y. J., Bodeker, G. E., Connor, B. J., Kampf, N., Hocke, K., Calisesi,
1085 Y., Schneider, N., de la Noe, J., Parrish, A. D., Boyd, I. S., Brühl, C., Steil, B., Giorgetta, M. A.,
1086 Manzini, E., Thomason, L. W., Zawodny, J. M., McCormick, M. P., Russell III, J. M., Bhartia,
1087 P. K., Stolarski, R. S., and Hollandsworth-Frith, S. M.: Long-term evolution of upper
1088 stratospheric ozone at selected stations of the Network for the Detection of Stratospheric Change
1089 (NDSC), *J. Geophys. Res.*, 111, D10308, doi:10.1029/2005JD006454, 2006a.

1090 Steinbrecht, W., Haßler, B., Brühl, C., Dameris, M., Giorgetta, M. A., Grewe, V., Manzini, E.,
1091 Matthes, S., Schnadt, C., Steil, B., and Winkler, P.: Interannual variation patterns of total ozone
1092 and lower stratospheric temperature in observations and model simulations, *Atmos. Chem. Phys.*,
1093 6, 349–374, doi:10.5194/acp-6-349-2006, 2006b.

1094 Steinbrecht, W., H. Claude, F. Schönenborn, I.S. McDermid, T. Leblanc, S. Godin-Beekmann,
1095 P. Keckhut, A. Hauchecorne, J.A.E. Van Gijssels, D.P.J. Swart, G.E. Bodeker, A. Parrish, I.S.
1096 Boyd, N. Kämpfer, K. Hocke, R.S. Stolarski, S.M. Frith, L.W. Thomason, E.E. Remsberg, C.
1097 Von Savigny, A. Rozanov, and J.P. Burrows, Ozone and temperature trends in the upper

1098 stratosphere at five stations of the Network for the Detection of Atmospheric Composition
1099 Change, *Int. J. Remote Sens.*, 30, 3875-3886, doi: 10.1080/01431160902821841, 2009.

1100 Stolarski, R. S. and Frith, S. M.: Search for evidence of trend slowdown in the long-term
1101 TOMS/SBUV total ozone data record: the importance of instrument drift uncertainty, *Atmos.*
1102 *Chem. Phys.*, 6, 4057–4065, 2006.

1103 Tian, W., Chipperfield, M. P., Gray, L. J., and Zawodny, J. M.: Quasi-biennial oscillation and
1104 tracer distributions in a coupled chemistry-climate model, *J. Geophys. Res.*, 111, D20301,
1105 doi:10.1029/2005JD006871, 2006.

1106 Varai, A., Homonnai, V., Jánosi, I.M., Müller, R. : Early signatures of ozone trend reversal over
1107 the Antarctic, *Earth's Future*, 3, 3, 95–109, doi:10.1002/2014EF000270, 2015.

1108 Vigouroux C., M. De Mazière, P. Demoulin, C. Servais, F. Hase, T. Blumenstock, I. Kramer, M.
1109 Schneider, J. Mellqvist, A. Strandberg, V. Velasco, J. Notholt, R. Sussmann, W. Stremme, A.
1110 Rockmann, T. Gardiner, M. Coleman, and P. Woods, Evaluation of tropospheric and
1111 stratospheric ozone trends over Western Europe from ground-based FTIR network observations,
1112 *Atmos. Chem. Phys.*, 8 (23), 6865-6886, doi: 10.5194/acp-8-6865-2008, 2008.

1113 Vigouroux, C., T. Blumenstock, M. Coffey, Q. Errera, O. García, N. B. Jones, J. W. Hannigan,
1114 F. Hase, B. Liley, E. Mahieu, J. Mellqvist, J. Notholt, M. Palm, G. Persson, M. Schneider, C.
1115 Servais, D. Smale, L. Thölix, and M. De Mazière: Trends of ozone total columns and vertical
1116 distribution from FTIR observations at 8 NDACC stations around the globe, *Atmos. Chem.*
1117 *Phys. Discuss.*, 14, 24623–24666, 2014.

1118 Weatherhead, E. C. and Andersen, S. B.: The search for signs of recovery of the ozone layer,
1119 *Nature*, 441, 39–45, doi:10.1038/nature04746, 2006.

1120 Weiss, A.K., J. Staehelin, C. Appenzeller, and N.R.P. Harris, Chemical and dynamical
1121 contributions to ozone profile trends of the Payerne (Switzerland) balloon soundings, *J.*
1122 *Geophys. Res.*, 106 (D19), 22685-22694, 2001.

1123 Wespes, C., Hurtmans, D., Clerbaux, C., Santee, M. L., Martin, R. V., and Coheur, P. F.: Global
1124 distributions of nitric acid from IASI/MetOP measurements, *Atmos. Chem. Phys.*, 9, 7949–7962,
1125 doi:10.5194/acp-9-7949-2009, 2009.

1126 Wespes, C., L. Emmons, D. P. Edwards, J. Hannigan, D. Hurtmans, M. Saunois, P.-F. Coheur,
1127 C. Clerbaux, M. T. Coffey, R. L. Batchelor, R. Lindenmaier, K. Strong, A. J. Weinheimer, J. B.

1128 Nowak, T. B. Ryerson, J. D. Crouse, and P. O. Wennberg: Analysis of ozone and nitric acid in
1129 spring and summer arctic pollution using aircraft, ground-based, satellite observations and
1130 mozart-4 model: source attribution and partitioning, *Atmos. Chem. Phys.*, 12, 237-259, 2012.

1131 Wilson, R. C., Fleming, Z. L., Monks, P. S., Clain, G., Henne, S., Kononov, I. B., Szopa, S.,
1132 and Menut, L.: Have primary emission reduction measures reduced ozone across Europe? An
1133 analysis of European rural background ozone trends 1996–2005, *Atmos. Chem. Phys.*, 12, 437–
1134 454, doi:10.5194/acp-12-437-2012, 2012.

1135 WMO: Scientific Assessment of Ozone Depletion: 2002, Global Ozone Research and
1136 Monitoring Project –Report No. 47, World Meteorological Organization, Geneva, Switzerland,
1137 2003.

1138 WMO: Scientific Assessment of Ozone Depletion: 2006, Global Ozone Research and
1139 Monitoring Project– Report 50, World Meteorological Organization, Geneva, Switzerland, 2007.

1140 WMO: Scientific Assessment of Ozone Depletion: 2010, Global Ozone Research and
1141 Monitoring Project–Report 52, World Meteorological Organization), Geneva, Switzerland, 2011.

1142 WMO : Scientific Assessment of Ozone Depletion: 2014, Global Ozone Research and
1143 Monitoring Project– Report 56, World Meteorological Organization, Geneva, Switzerland, 2014.

1144 Yang, E.-S., Cunnold, D. M., Salawitch, R. J., McCormick, M. P., Russell, J., Zawodny, J. M.,
1145 Oltmans, S., and Newchurch, M. J.: Attribution of recovery in lower-stratospheric ozone, *J.*
1146 *Geophys. Res.*, 111, D17309, doi:10.1029/2005JD006371, 2006.

1147

1148

1149

1150

1151

1152

1153

1154

1155

1156

1157

1158 **Table 1** List of the proxies used in this study and their sources

Proxy	Description (<i>resolution</i>)	Sources
F10.7	The 10.7 cm solar radio flux (<i>daily or monthly</i>)	NOAA National Weather Service Climate Prediction Center: ftp://ftp.ngdc.noaa.gov/STP/space-weather/solar-data/solar-features/solar-radio/noontime-flux/penticton/penticton_adjusted/listings/listing_drao_noontime-flux-adjusted_daily.txt or ftp://ftp.ngdc.noaa.gov/STP/space-weather/solar-data/solar-features/solar-radio/noontime-flux/penticton/penticton_adjusted/listings/listing_drao_noontime-flux-adjusted_monthly.txt
QBO¹⁰ QBO³⁰	Quasi-Biennial Oscillation index at 10hPa and 30hPa (<i>monthly</i>)	Free University of Berlin: www.geo.fu-berlin.de/en/met/ag/strat/produkte/qbo/
ENSO	El Niño /Southern Oscillation - Nino 3.4 Index (<i>3-monthly averages</i>)	NOAA National Weather Service Climate Prediction Center: http://www.cpc.noaa.gov/data/indices/
NAO	North Atlantic Oscillation index (<i>daily or monthly</i>)	ftp://ftp.cpc.ncep.noaa.gov/cwlinks/norm.daily.nao.index.b500101.current.ascii or http://www.cpc.ncep.noaa.gov/products/precip/CWlink/pna/norm.nao.monthly.b5001.current.ascii
AAO	Antarctic Oscillation index (<i>daily or monthly</i>)	ftp://ftp.cpc.ncep.noaa.gov/cwlinks/norm.daily.aao.index.b790101.current.ascii or http://www.cpc.ncep.noaa.gov/products/precip/CWlink/daily_ao_index/aao/monthly.aao.index.b79.current.ascii

1159
1160
1161
1162
1163
1164
1165
1166
1167
1168
1169
1170
1171
1172
1173
1174

1175 **Table 2** Ozone trends and associated uncertainties (95% confidence limits; accounting for the
1176 autocorrelation in the noise residuals), given in DU/year, for 20-degree latitude bands, based on
1177 daily (top values) and monthly (bottom values) medians over 6 years of IASI observations. Bold
1178 (underlined) values refer to significant (positive) trends. Values marked with a star (*) refer to
1179 trends which are rejected by the iterative backward elimination procedure[†].

<i>DU/yr</i>	# Days	Ground-300hPa (MLT)	300-150hPa (UTLS)	150-25hPa (MLST)	25-3hPa (UST)	Total columns
70°N-90°N (Feb-Oct)	1493	-0.13±0.10	<u>1.28±0.82</u>	<u>2.81±2.27</u>	-0.16±0.97*	<u>3.90±2.93</u>
		-0.03±0.29*	0.70±0.92	-0.04±2.60	-1.81±2.81*	1.37±3.62*
50°N-70°N	2103	-0.08±0.09	<u>0.73±0.51</u>	0.97±1.30	<u>0.55±0.36</u>	<u>1.93±1.71</u>
		0.17±0.35*	1.24±1.24	2.28±4.24*	0.66±0.76	4.72±5.58
30°N-50°N	2105	-0.19±0.05	<u>0.34±0.18</u>	-0.34±0.77	<u>0.89±0.41</u>	0.91±1.24
		-0.15±0.13	<u>0.75±0.75</u>	-0.37±1.65*	<u>0.87±0.52</u>	0.33±2.25*
10°N-30°N	2105	0.10±0.11	-0.03±0.10*	-0.73±0.29	<u>0.95±0.65</u>	0.21±0.30*
		0.12±0.15*	0.05±0.12*	-0.55±0.62*	<u>1.25±0.74</u>	0.82±1.01
10°S-10°N	2104	-0.41±0.12	-0.25±0.07	-0.11±0.26*	<u>0.44±0.19</u>	-0.16±0.34
		-0.25±0.14	-0.08±0.10	-0.11±0.64*	0.61±0.64	0.13±0.83*
30°S-10°S	2106	-0.22±0.10	-0.08±0.04	-0.61±0.26	<u>0.89±0.58</u>	-0.04±0.31*
		-0.15±0.13	-0.09±0.07	-0.45±0.36	0.80±1.23	-0.01±1.26*
50°S-30°S	2105	-0.19±0.07	-0.22±0.08	-2.17±0.58	<u>1.74±0.77</u>	-0.79±0.96
		-0.18±0.09	-0.27±0.12	-2.36±1.80	1.21±1.30	-0.64±1.45*
70°S-50°S	2105	-0.13±0.05	0.09±0.16	0.56±0.82	<u>0.54±0.29</u>	1.15±1.28
		-0.22±0.12	0.05±0.32*	0.02±1.15*	0.57±0.82	0.51±1.75*
90°S-70°S (Oct-Apr)	738	-0.15±0.21*	0.01±0.61*	0.00±2.36*	<u>1.04±0.57</u>	1.50±3.15*
		-0.17±0.40*	0.25±0.73*	2.59±3.80*	0.91±2.10	3.28±5.12*

1180 † The trend values result from the adjustment of the regression model where the linear term is
1181 kept whatever its p-value calculated during the iterative process.

1182
1183
1184
1185
1186
1187
1188

1189 **Table 3** Same as Table 2 but for seasonal O₃ trends and associated uncertainties based on daily
 1190 medians during JJA (top values) and DJF (bottom values) periods. Values marked with a star (*)
 1191 refer to trends which are rejected by the iterative backward elimination procedure[†].

<i>DU/yr</i>	# Days	Ground-300hPa (MLT)	300-150hPa (UTLS)	150-25hPa (MLST)	25-3hPa (UST)	Total columns
70°N-90°N (Feb-Oct)	613 48	-0.18±0.08	<u>1.13±0.65</u>	-0.91±1.52	<u>1.72±0.51</u>	1.36±1.15
		-	-	-	-	-
50°N-70°N	551 527	-0.23±0.07 -0.09±0.12*	<u>1.03±0.37</u> <u>1.74±1.30</u>	0.62±1.64 0.73±1.73*	<u>1.67±0.48</u> -0.66±0.79	3.01±1.64 1.56±2.66*
30°N-50°N	551 529	-0.30±0.10 -0.24±0.09	<u>0.42±0.30</u> 0.28±0.28	-0.30±0.65* -0.82±0.90	<u>0.84±0.25</u> <u>0.62±0.49</u>	1.17±1.35 -0.81±1.05
10°N-30°N	551 529	-0.05±0.16* <u>0.18±0.14</u>	<u>0.17±0.05</u> 0.01±0.09*	-0.34±0.30 -1.05±0.45	<u>0.36±0.27</u> 0.49±0.54	-0.09±0.54* -1.14±0.44
10°S-10°N	551 529	-0.06±0.10 -0.70±0.23	0.04±0.05* -0.32±0.10	-0.84±0.86 1.64±1.77	0.32±0.42 0.53±0.59	-0.56±0.74* 0.34±0.93*
30°S-10°S	551 530	-0.26±0.09 -0.15±0.11	-0.06±0.07 0.06±0.12*	-0.56±0.40 -0.12±0.31*	<u>1.06±0.55</u> <u>1.48±0.53</u>	0.24±0.43 <u>1.56±0.92</u>
50°S-30°S	551 529	-0.21±0.05 -0.10±0.06	-0.16±0.09 -0.14±0.06	-0.52±0.54 -2.83±0.64	0.49±0.59 <u>3.40±0.85</u>	-0.44±0.83 0.47±0.52
70°S-50°S	551 529	-0.25±0.06 -0.10±0.04	1.03±0.60 0.19±0.24*	<u>2.63±1.65</u> <u>0.52±0.48</u>	<u>0.98±0.62</u> <u>1.66±0.70</u>	<u>3.44±2.47</u> <u>1.72±0.74</u>
90°S-70°S (Oct-Apr)	- 523	- -0.21±0.20	- -0.46±0.80*	- 0.16±2.53*	- <u>1.18±0.67</u>	- 0.98±3.27*

1192 † The trend values result from the adjustment of the regression model where the linear term is
 1193 kept whatever its p-value calculated during the iterative process.

1194
 1195
 1196
 1197
 1198
 1199
 1200
 1201

1202 **Table 4** Ozone trends and associated uncertainties (95% confidence limits), given in DU/year
1203 over NDACC (Network for the Detection of Atmospheric Composition Change) stations in the
1204 N.H. based on daily medians of IASI (within a grid box of 1°x1° centered on stations, two first
1205 rows) and FTIR observations (successive rows for different time intervals). Italic values (2^d row)
1206 refer to trends inferred from subsampled IASI data and bold values refer to statistically
1207 significant trends. Values marked with a star (*) refer to trends which are rejected by the iterative
1208 backward elimination procedure[†].

<i>DU/yr</i>	Data periods	# days	25-3hPa (US)	Total columns
Ny-Alesund (79°N) Mar-Sept	2008-2013	1239	0.56±0.73	5.26±4.72
	<i>Subsamp.</i> 2008-2012	82	<i>-0.29±4.58</i>	<i>6.26±18.11</i>
	2008-2012	84	-3.58±4.58	2.24±20.78*
	2003-2012	168	-0.17±0.70*	-4.84±3.01
	2000-2012	288	0.64±0.60	-1.02±2.40*
	1999-2012	320	0.62±0.55	-2.35±1.40
	1995-2012	383	1.03±0.66	1.31±2.39*
	1995-2003	167	1.25±1.05	3.33±3.41
Thule (77°N) Mar-Sept	2008-2013	1094	1.24±1.09	4.97±4.72
	<i>Subsamp.</i> 2008-2012	231	<i>1.31±2.69</i>	<i>0.10±7.36</i>
	2008-2012	340	-2.10±2.89	0.39±11.59*
	2003-2012	697	0.86±0.89	-2.77±2.99
	2000-2012	776	1.33±0.86	-1.29±1.73
	1999-2012	779	1.69±0.88	-1.25±1.74
	1999-2003	138	3.73±2.90	-1.25±1.74*
				4.86±10.13*
Kiruna (68°N) Mar-Sept	2008-2013	1236	0.21±1.42	4.41±4.00
	<i>Subsamp.</i> 2008-2012	226	<i>0.97±4.05</i>	<i>3.78±6.03</i>
	2008-2012	254	-1.97±6.04*	-3.75±6.64*
	2003-2012	678	0.15±0.67*	2.26±3.68
	2000-2012	913	1.60±1.29	3.69±4.20
	1999-2012	984	1.10±0.98	-0.43±1.64*
	1996-2012	1183	1.11±0.54	1.82±1.77
	1996-2003	596	1.26±1.21	1.12±3.77*
Jungfraujoch (47°N)	2008-2013	1580	2.95±0.61	5.64±3.15
	<i>Subsamp.</i> 2008-2012	524	<i>3.72±1.14</i>	<i>5.61±5.11</i>
	2008-2012	565	1.60±1.80	5.28±4.82
	1998-2012	1582	0.10±0.35	-0.28±0.86*
	1995-2012	1771	0.02±0.33*	0.85±0.79

Zugspitze (47°N)	2008-2013	1729	3.17±0.56	5.53±2.92
	<i>Subsamp.</i>			
	2008-2012	538	3.56±1.63	5.99±4.49
	2008-2012	597	0.71±1.22	3.46±3.79
	1998-2012	1472	0.08±0.32*	0.81±0.98
	1995-2012	1525	0.23±0.32	1.36±1.01
Izana (28°N)	2008-2013	1803	0.56±0.65	1.28±0.77
	<i>Subsamp.</i>			
	2008-2012	380	0.32±1.28	0.11±1.95
	2008-2012	443	0.24±0.80*	0.91±2.44*
	1999-2012	1257	0.46±0.25	0.20±0.33*

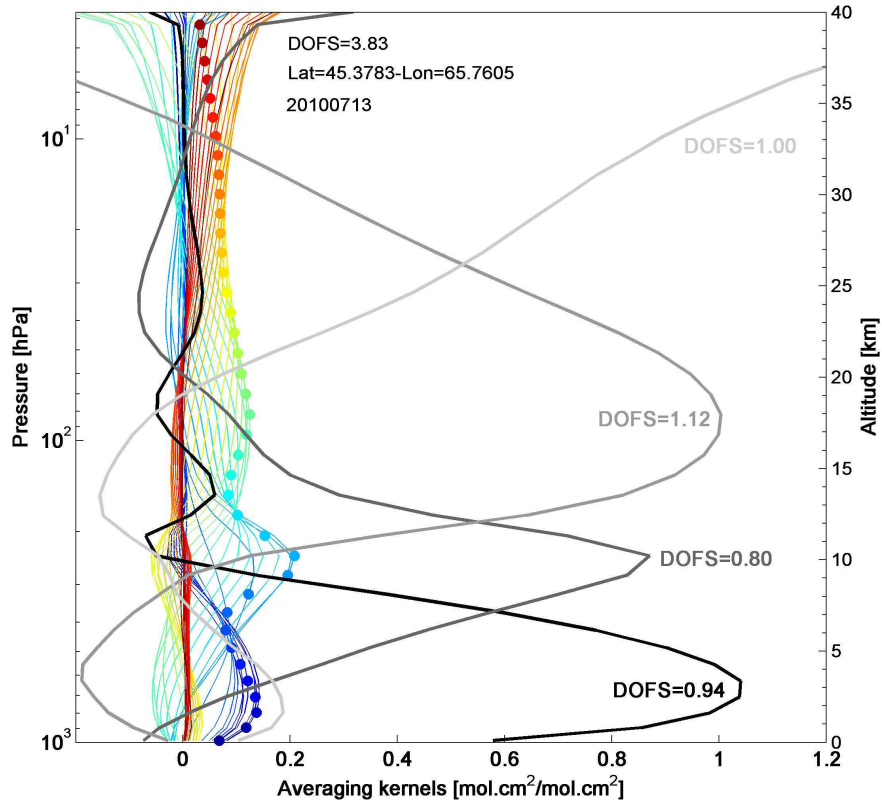
1209 † The trend values result from the adjustment of the regression model where the linear term is
1210 kept whatever its p-value calculated during the iterative process.

1211
1212
1213
1214
1215
1216
1217
1218
1219
1220
1221
1222
1223
1224
1225
1226
1227
1228
1229
1230

1231

1232

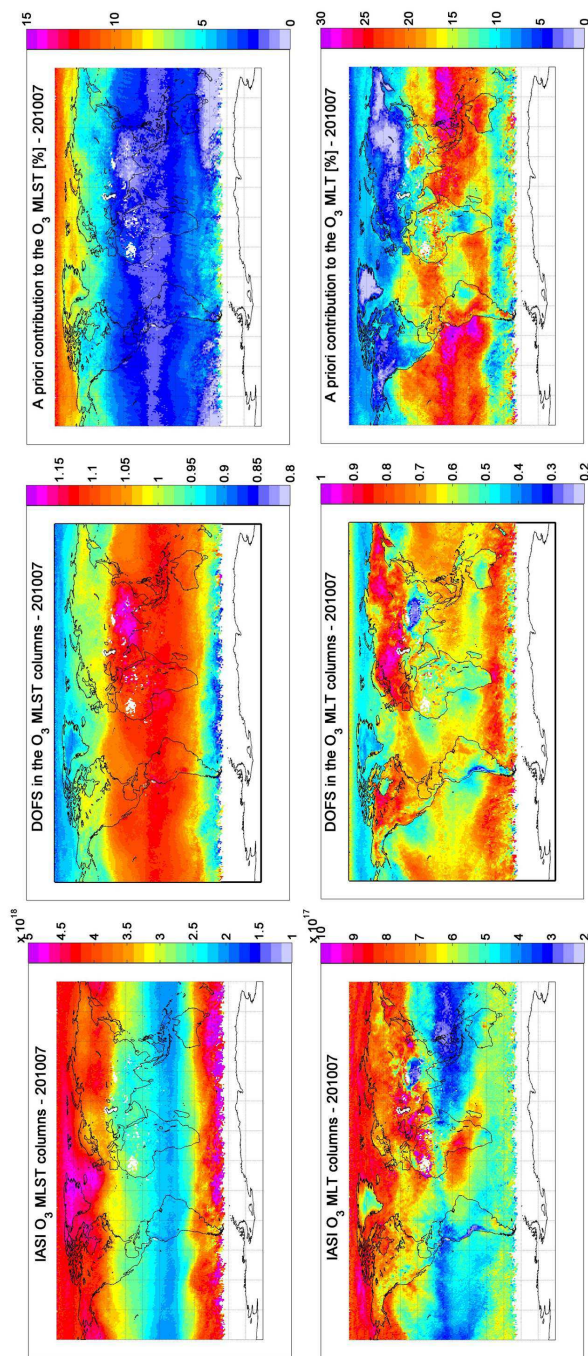
1233 **Figure captions**



1234

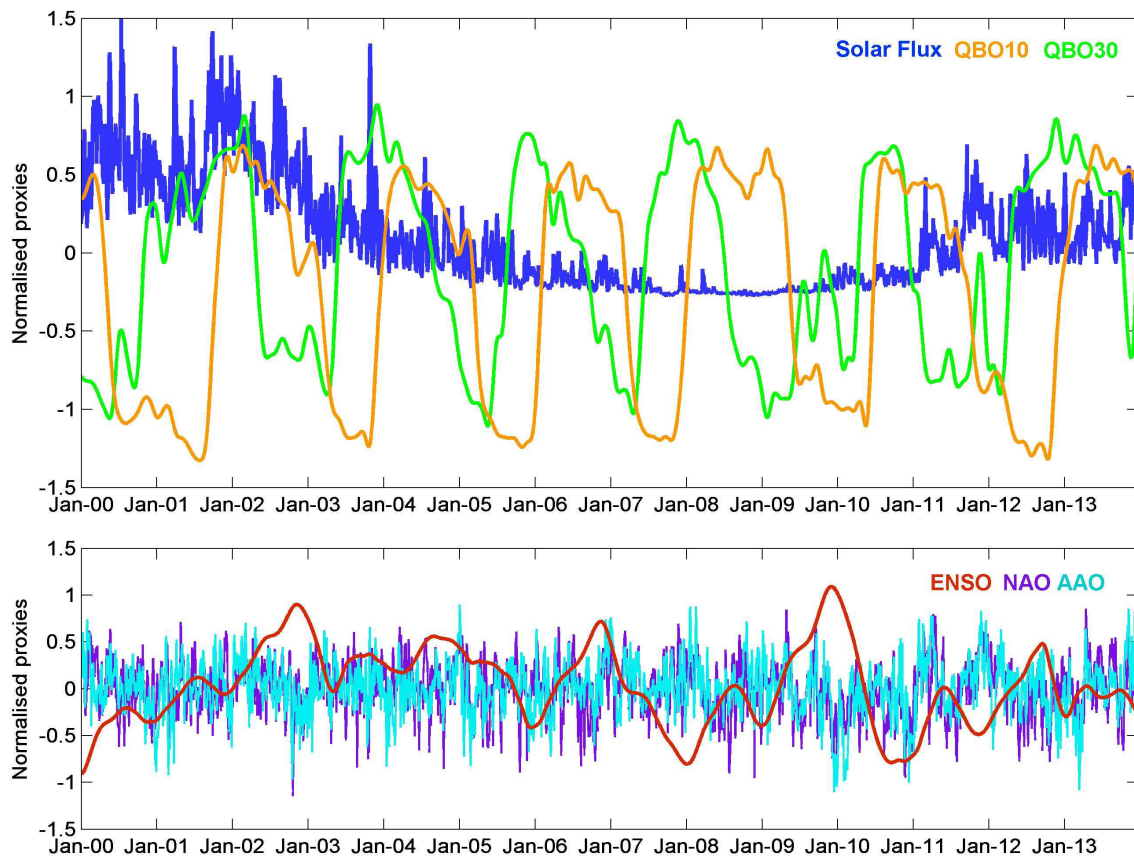
1235 **Figure 1.** Typical IASI FORLI-O₃ averaging kernels, in partial column units, corresponding to
1236 one mid-latitude observation in July (45°N/66°E) for each 1 km retrieved layers from ground to
1237 40 km altitude (color scale) and for 4 merged layers: ground-300 hPa; 300-150 hPa; 150-25 hPa;
1238 25-3 hPa (grey lines). The total DOFS and the DOFS for each merged layers are also indicated.

1239



1240

1241 **Figure 2.** Distributions of (a) O₃ columns, (b) DOFS and (c) *a priori* contribution (given as a %)
 1242 in the ground-300hPa (MLT) and 150-25hPa (MLST) layers for IASI O₃, averaged over July
 1243 2010 daytime data. Note that the scales are different.



1244

1245 **Figure 3.** Normalized proxies as a function of time for the period 2000-2013 for the solar F10.7
 1246 cm radio flux (blue) and the equatorial winds at 10 (green) and 30 hPa (orange), respectively (top
 1247 panel), and for the El Niño (red), north Atlantic oscillation (purple) and Antarctic oscillation
 1248 (light blue) indexes (bottom panel).

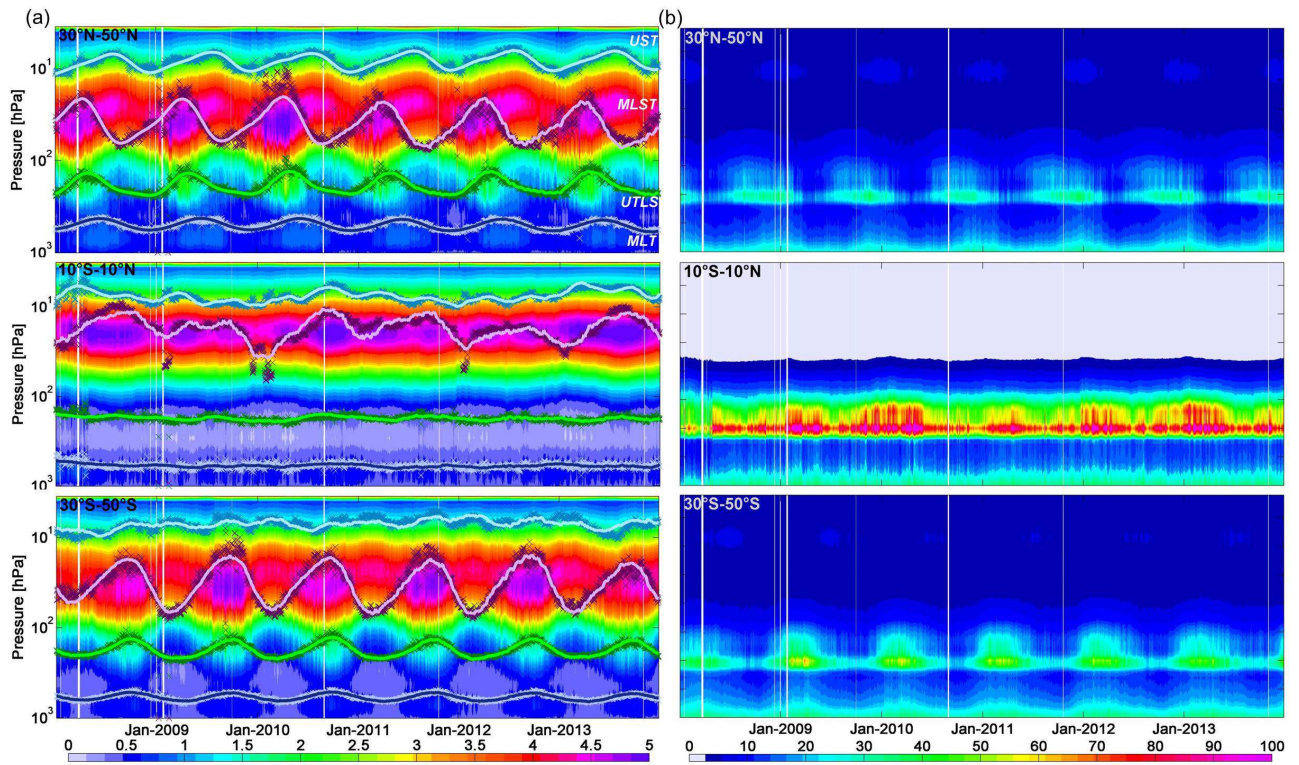
1249

1250

1251

1252

1253



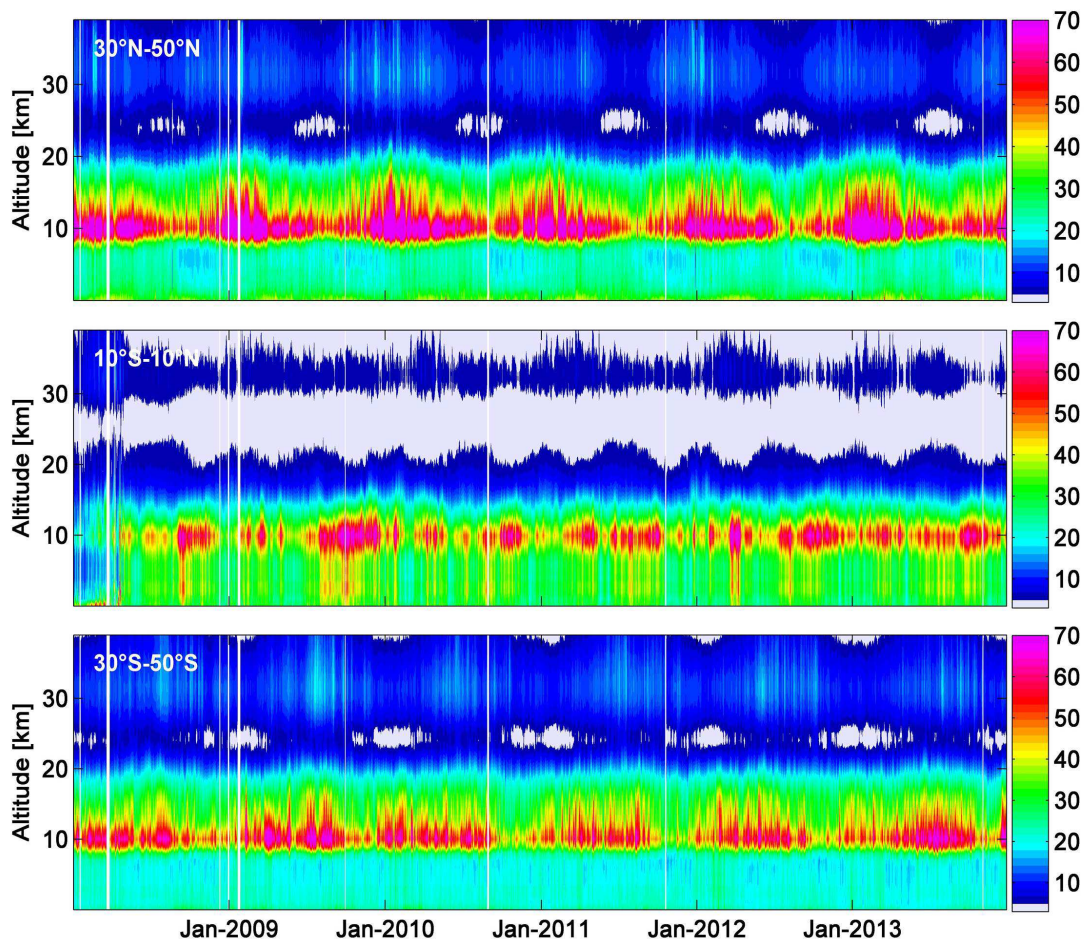
1254

1255 **Figure 4.** (a) Daily IASI O₃ profiles (1×10^{12} molecules/cm³) for the period 2008-2013 and over
 1256 the range of the retrieved profiles as a function of time and altitude, in three latitude bands:
 1257 30°N-50°N (top), 10°S-10°N (middle), 30°S-50°S (bottom). Superimposed daily IASI O₃ partial
 1258 columns (scatters) and the associated fits (solid lines) from the multivariate regressions for the
 1259 MLT (ground-300hPa), UTLS (300-150hPa), MLST (150-25hPa) and UST (above 25hPa)
 1260 layers. The IASI measurements and the fits have been scaled for clarity. (b) Estimated total
 1261 retrieval errors (%) associated with daily IASI O₃ profiles.

1262

1263

1264



1265

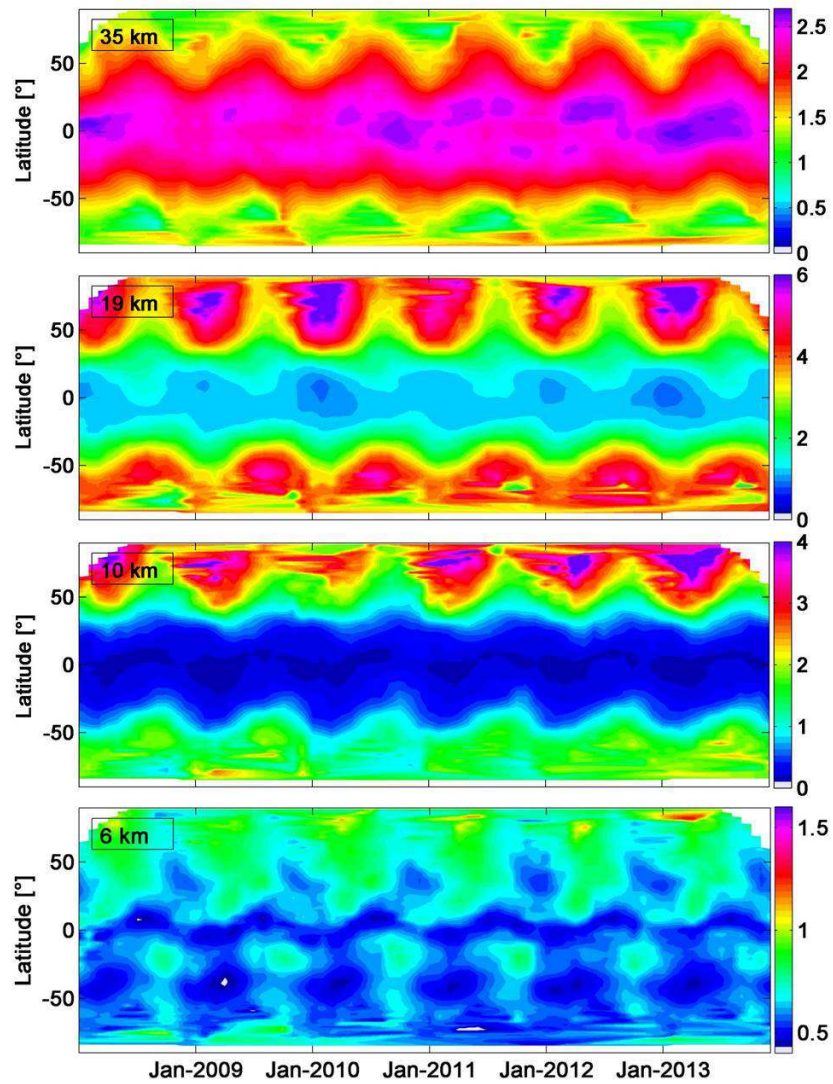
1266 **Figure 5.** Daily IASI O₃ variability (%), expressed as $[\sigma(O_3(t))/O_3(t)]100\%$, where σ is the
 1267 standard deviation, as a function of time and altitude in three latitude bands: 30°N-50°N (top),
 1268 10°S-10°N (middle), 30°S-50°S (bottom).

1269

1270

1271

1272



1273

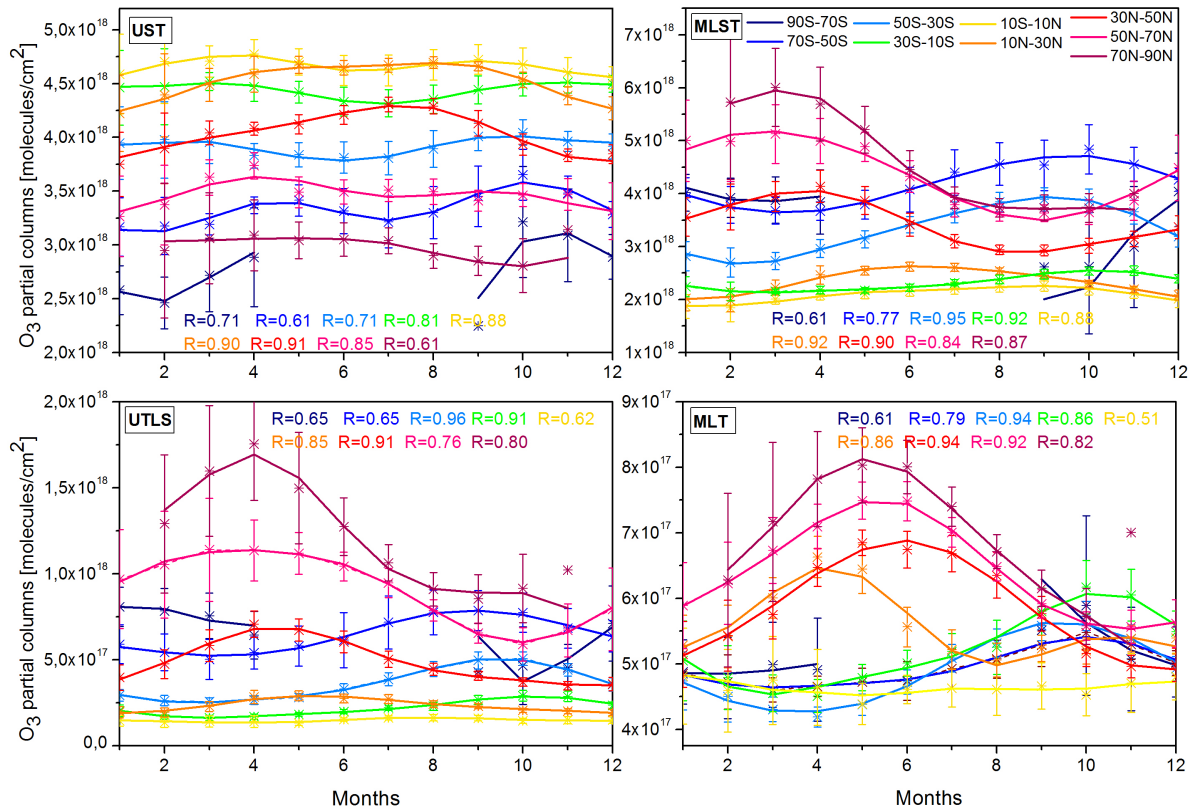
1274 **Figure 6.** Daily IASI O₃ number density (1×10^{12} molecules/cm³) at 35 km (top row), 19 km
 1275 (second row), 10 km (third row) and 6 km (bottom row) as a function of time and latitude. Note
 1276 that the color scales are different.

1277

1278

1279

1280



1281

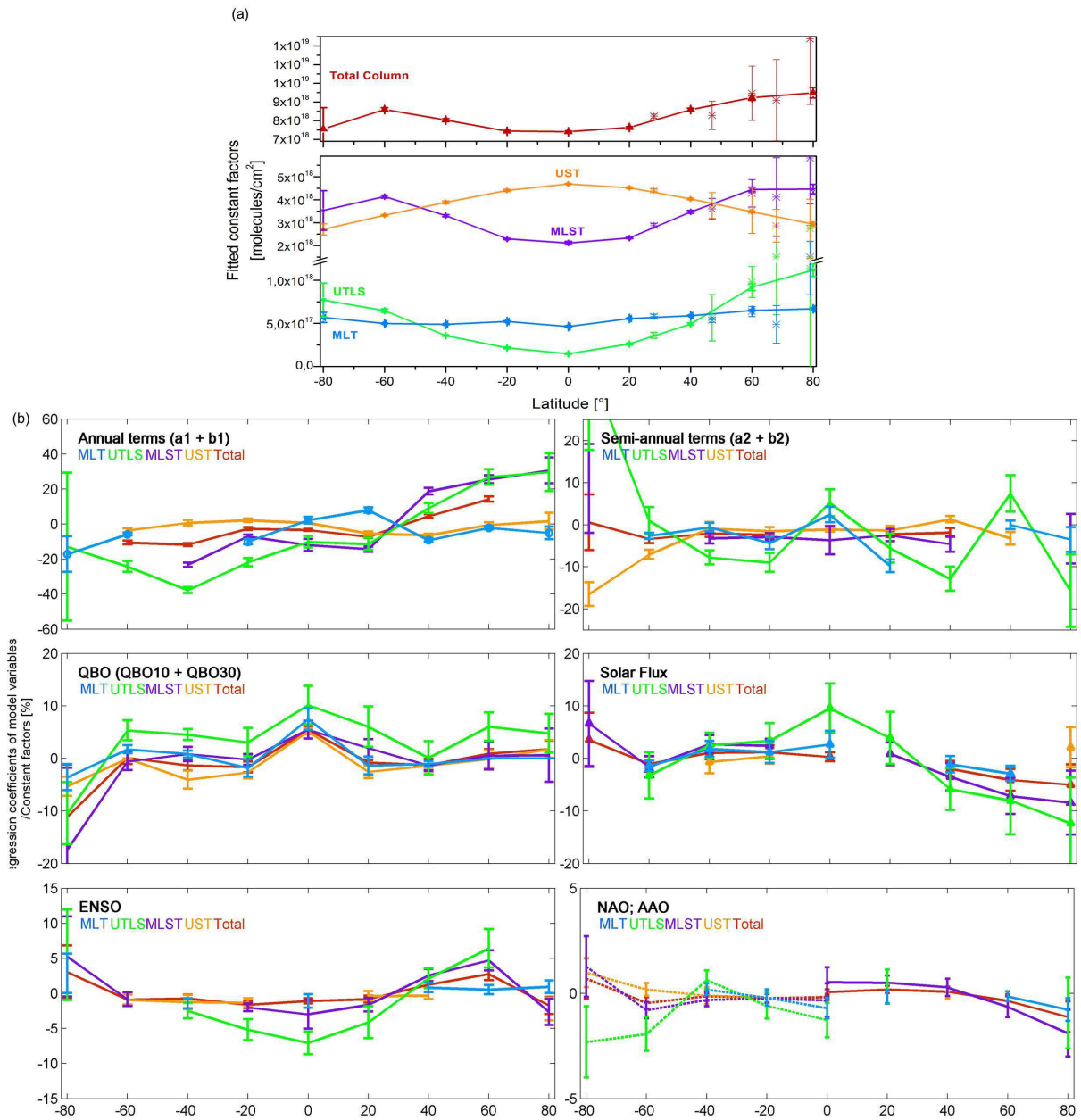
1282 **Figure 7.** Monthly medians of measured (scatters) and of fitted (line) IASI O₃ columns averaged
 1283 over the period 2008-2013, for the UST, MLST, UTLS and MLT layers and for each 20-degrees
 1284 latitude bands (color scale in the top-right panel). The fit is based on daily medians. Error bars
 1285 give the 1 σ standard deviation relative to the monthly median values. Correlation coefficient (R)
 1286 between the daily median observations and the fit are also indicated. Note that the scales are
 1287 different.

1288

1289

1290

1291



1292

1293

1294

1295

1296

1297

1298

Figure 8. (a) Fitted constant factors (Cst, see Eq.1, Section 3) from the 6-years IASI daily O₃ time series for the 20-degree latitude belts, separately given for the 4 layers and for the total column. The stars correspond to the constant factors fitted above ground-based measurement stations: Ny-Ålesund (79°N), Kiruna (68°N), Harestua (60°N), Jungfraujoch (47°N), Izana (28°N). (b) Regression coefficients of the variables retained by the stepwise procedure, given in % as [(regression_coefficients)]/fitted_Cst]x100%. Identification for the variables: Annual (top

1299 left) and Semi-Annual variations (top right) terms, QBO at 10 and 30 hPa (bottom left), solar
1300 flux (bottom right). Note that the scales are different. The associated fitting uncertainties (95%
1301 confidence limits) are also represented (error bars).

1302

1303

1304

1305

1306

1307

1308

1309

1310

1311

1312

1313

1314

1315

1316

1317

1318

1319

1320

1321

1322

1323

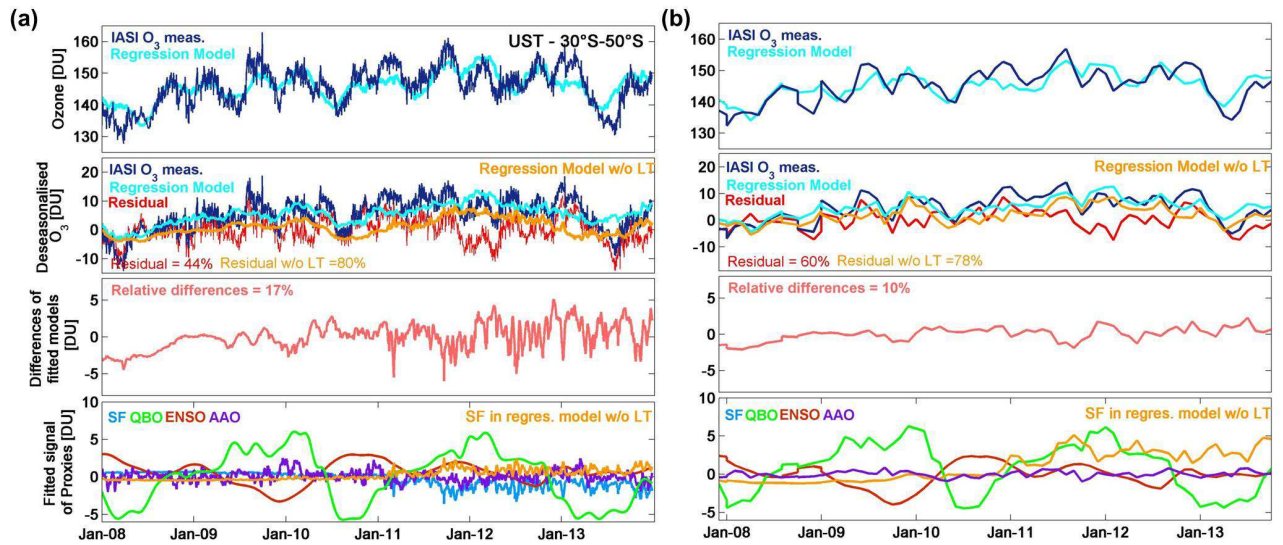
1324

1325

1326

1327

1328



1329

1330 **Figure 9.** Daily (a) and monthly (b) time series of O₃ measurements and of the fitted regression
 1331 model in the UST for the 30°S-50°S latitude band (top row), of the deseasonalised O₃ (2^d row),
 1332 of the difference of the fitted models with and without the linear term (3^d row), and of the fitted
 1333 signal of proxies ([regression coefficients*Proxy]): SF (blue), QBO (QBO¹⁰ + QBO³⁰; green),
 1334 ENSO (red) and AAO (purple) (bottom) (given in DU). The averaged residuals relative to the
 1335 deseasonalised IASI time series are also indicated (%).

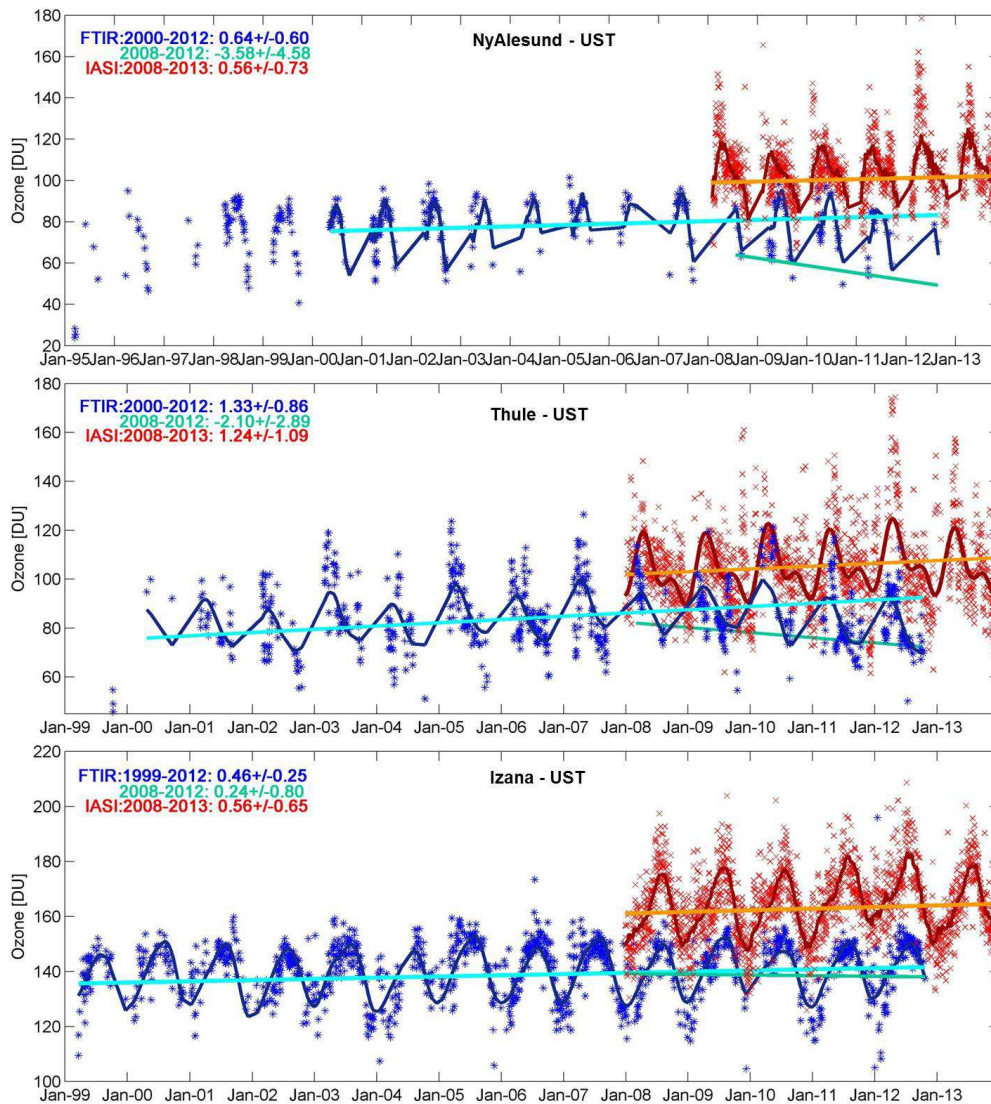
1336

1337

1338

1339

1340



1341
 1342 **Figure 10.** Daily time series of O₃ FTIR (blue symbols) and IASI (red symbols) measurements in
 1343 the UST at Ny-Alesund (top), Thule (middle) and Izana (bottom), covering the 1995-2012 and
 1344 the 1999-2012 periods, respectively (given in DU). The fitted regression models (dark blue and
 1345 dark red lines, for FTIR and IASI, respectively) and the linear trends calculated for periods
 1346 starting after the turnaround over 1999/2000-2012 and over 2008-2012 for FTIR (light blue and
 1347 green lines), and the 2008-2013 period for IASI (orange line) are also represented (DU/yr). The
 1348 trend values given in DU/year are indicated.
 1349